EUMETSAT ECMWF

EUMETSAT/ECMWF Fellowship Programme
Research Report

RR61

Microwave Imagers in the ECMWF-IFS: Adding further observations and improving convective anvils in the observation operator

Tracy Scanlon, Alan Geer, Niels Bormann

April 2023

Series: EUMETSAT/ECMWF Fellowship Programme Research Reports

A full list of ECMWF Publications can be found on our web site under:
http://www.ecmwf.int/en/publications/

Contact: library@ecmwf.int

European Centre for Medium Range Weather Forecasts, Shinfield Park, Reading, RG2 9AX, UK

Contents

Executive Summary

Observations from microwave imagers provide a significant contribution to the European Centre for Medium Range Weather Forecasts Integrated Forecast System (ECMWF-IFS). Continued development of the framework that utilises these observations ensures that current and future instruments can be exploited to their full potential. In particular, the work in this study will benefit the upcoming EUMETSAT Polar System - Second Generation (EPS-SG) Microwave Imager (MWI) as well as the Ice Cloud Imager (ICI). This report focuses on the microwave imager data being assimilated (both in terms of instruments and frequencies) and the simulation of Brightness Temperatures (TBs) for comparison to the observations.

In this report, the use of data from previously unexploited channels of Special Sensor Microwave - Imager/Sounder (SSMIS) on board Defense Meteorological Satellite Program (DMSP) F18 (SSMIS-F18) is considered and it is found that there are some unexplained artefacts in the data relating to the use of the 37.0v GHz channel. These artefacts result in a 1.85 K bias between the ascending and descending nodes in the Southern Hemisphere winter. Excluding this channel and applying an Ascending / Descending (A/D) bias predictor reduces the adverse effects of including SSMIS-F18 on the 12 hour to 3 day forecast. Instead, the new channels give improved wind and humidity forecasts in the short range. Hence it is recommended that SSMIS-F18 be included into the ECMWF-IFS in this configuration.

The orbital biases seen in Microwave Radiation Imager (MWRI) on-board Fengyun-3D (FY-3D) are also discussed and it is demonstrated why this instrument has been removed from ECMWF operations from May 2022 onwards. A correction implemented by China Meteorological Administration (CMA) has resulted in a reduction but not elimination of the A/D biases, however, as these are still present the data will not be re-introduced into the operational system at this time.

This report also considers the inclusion of the 37h and 89h GHz-polarisation channels, which should bring new information on humidity and cloud. This is tested for currently assimilated microwave instruments. However, it is found that inclusion of the channels individually and together both results in degradation of the fit of the model to observations as well as the degradation of the forecast scores. This suggests that further development is required before these channels can be used, for example by improving observation error modelling or reducing systematic errors in the model.

In terms of improving the simulated TBs, a new hydrometeor fraction assumption has been tested, which models the convective precipitation fraction as linearly changing from the bottom to the top of the frozen part of an anvil cloud. This results in improvements in particular for the case where there were extreme differences between the observations and simulated TBs of up to $\pm$ 40 K; these improvements can be most clearly seen in the reduced skewness of the First Guess (FG) departures. Although these changes affect only a small number of observations, due to the large magnitude of the changes it will be implemented as part of a future version of the ECMWF-IFS.

Finally, the impact of extending the range of both the Liquid Water Content (LWC) and temperatures in the tables used for the optical properties in the simulation of TBs has been tested. This work is particularly important to support the upcoming missions for EUMETSAT, including ICI. These have been shown to have a minimal impact on the simulated TBs, however in the future the extended temperature will become important, therefore, the functionality to allow this extension will be added to the RTTOV software package.

Plain Language Summary

Observations from microwave instruments are a vital part of the European Centre for Medium Range Weather Forecasts (ECMWF) forecast system. Ongoing improvements are being made to the way in which these are used in the system to support currently and future instruments. This report presents two facets of this work: the inclusion / exclusion of data and the improvement of simulated values which the observations are compared with as part of the forecast process. The work presented in this report shows that, in a particular configuration, previously unexploited channels from Special Sensor Microwave - Imager/Sounder (DMSP SSMIS-F18 (SSMIS-F18)) can now be included into the system, but unfortunately, data from Microwave Radiation Imager (MWRI) has been removed from operations, with ongoing monitoring. There has also been an attempt to include previously unexploited H-polarised channels, however this resulted in a degradation to the forecast and is not considered further. In addition, the report describes changes to the cloud fraction assumption for the frozen part of anvil clouds, which results in the reduction of some extreme differences between the simulated and observed Brightness Temperatures (TBs). Lastly, the range covered by lookup tables used in the generation of the simulated TBs are assessed and it is decided that functionality for a wider range will be provided in the software but not operationally implemented.

1 Introduction

Data from microwave imagers have been proven to improve atmospheric humidity, cloud and precipitation analysis in operational Numerical Weather Prediction (NWP) systems. At the European Centre for Medium Range Weather Forecasts (ECMWF), 4 microwave imagers (see Table 1) are, or have been, actively assimilated into the Integrated Forecast System (IFS) under all-sky (clear and cloudy) conditions (Bauer *et al.*, 2010; Geer *et al.*, 2010b; Geer and Bauer, 2010, 2011). An up-to-date summary of the utilisation of microwave imagers at ECMWF can be found in Geer *et al.* (2022).

Efforts are on-going to improve how microwave imagers are used within the ECMWF-IFS and to further exploit the information available from these sensors. This includes the consideration (and potential introduction) of microwave imagers not yet exploited within the system. Related to this is the continual monitoring of the sensors already in the system to ensure they continue to provide benefit to the operational forecast. It is also important to make better use of the sensors that are already actively assimilated. There are varied ways to achieve this but one focus is more realistically modelling the simulated Brightness Temperatures (TBs) within the observation operator with the aim of reducing the departures between these and the observed TBs. The work presented contributes to preparations for the EPS-SG MWI and ICI instruments, as well as other planned microwave imagers.

In this report, we focus on three themes: the addition and maintenance of microwave imagers (Section 2), improving the way in which convective situations are represented in the observation operator (Section 3) and determining if the lookup tables used in the observation operator are sufficient (Section 4).

Note that, all of the experiments presented in this report were run over two seasons (June, July, August (JJA) 2020 and December, January, February (DJF) 2020/1) with the exception of the Microwave Radiation Imager (MWRI) experiments (Section 2.2) which were run for DJF 2021/2 and 2022/3. All experiments were run at a model resolution of TCo399 (29 km) with a final incremental analysis resolution of T_L255 (80 km) and 137 vertical levels. All experiments are based on CY47R3 with additions to the microwave elements of the system equivalent to CY48R1. In some instances, operational data is used for verification purposes; for more information on the set up of the operational forecast, please refer to Lean *et al.* (2021).

Table 1: Microwave imagers currently assimilated in the ECMWF-IFS. For acronyms, see WMO (2022c).

Sensor	**Platform**	**Dates**	**Notes**
SSMIS	DMSP-F17	2009-12 to present	Inclusion of data from DMSP-F18 is the subject of Section 2.1. The 37.0 and 91.655h GHz channels from SSMIS on-board DMSP-F17 are considered in Section 2.3.
GMI	GPM	2015-08 to present	The 36.5 and 89.0h GHz channels are considered in Section 2.3.
AMSR2	GCOM-W	2015-08 to present	The 36.5 and 89.0h GHz channels are considered in Section 2.3.
MWRI	FY-3D	2020-06 to 2022-05	The reasoning behind the removal of this data in May 2022 is the subject of Section 2.2. The 36.5 and 89.0h GHz channels are considered in Section 2.3.

2 Addition and Maintenance of Microwave Imagers

2.1 Inclusion of SSMIS-F18 imager channels

2.1.1 SSMIS within the ECMWF-IFS

The SSMIS instrument has been deployed on a series of satellites over the past 20 years: Defense Meteorological Satellite Program (DMSP-) F16 (2003-2019), F17 (2006-present), F18 (2009-present) and F19 (2014-2016) (WMO, 2022b). SSMIS is a conical microwave scanner with 24 channels ranging from 19 GHz to 183 GHz; a subset of these channels are used in the ECMWF-IFS.

Observational data from SSMIS on-board DMSP-F17 have been actively assimilated in an all-sky configuration into the ECMWF-IFS since December 2009. For this instrument, both the window channels as well as the humidity-sounding channels near 183 GHz are assimilated, whereas temperature-sounding channels in the 50 GHz band are not used operationally as they are considerably affected by instrument anomalies (Bell *et al.*, 2008). The impact of the DMSP-F17 observations can be measured using the Forecast Sensitivity Observation Impact (FSOI) metric (Cardinali, 2009) which shows that the microwave channels sensitive to water vapour and/or temperature together provide the largest impact on the operational forecast at ECMWF, approximately 33 % based on the 2022 calendar year. Of the instruments contributing to this, SSMIS-F17 is the largest contributor (approx. 2.8 %) for the channels sensitive to water vapour (and the 9th largest contributor overall). Therefore, further exploitation of similar channels could be beneficial to the ECMWF-IFS.

Although the DMSP-F18 platform was launched in October 2009, the imager channels from SSMIS-F18 (listed in Table 2) have not yet been actively assimilated into the operational forecast system as the satellite had been in a similar orbit to DMSP-F17 (Geer, 2013) and the SSMIS-F18 sensor had been shown to suffer from solar intrusions on the warm load reflector (see discussion later and Bell *et al.* (2008)). In the meantime, the orbits of DMSP-F17 and DMSP-F18 have drifted and are now more complementary (F17 is at 06:40 descending, whereas F18 is at 04:50 descending). It was hence decided to revisit this decision. This section presents the results of the work undertaken to determine if the SSMIS-F18 imager channels are suitable for inclusion within the ECMWF-IFS.

Table 2: SSMIS Channels to be tested for inclusion into the ECMWF-IFS from DMSP-F18.

Channel	Central Frequency [GHz]	Polarisation	Bandwidth [MHz]
12	19.35	H	356
13	19.35	V	356
14	22.235	V	407
16	37.0	V	1580
17	91.655	V	1580

Whilst the design of SSMIS has not substantially changed since the first instrument was launched in 2003 (on-board DMSP-F16), there are differences between instruments, as well as their mounting on the satellites and the orbits of those satellites (Kroodsma *et al.*, 2021). It is well known that SSMIS on-board DMSP-F16 suffered from radiometric calibration anomalies caused by solar illumination of the warm calibration load and the high emissivity of the reflector antenna (Bell *et al.*, 2008; Kunkee *et al.*, 2008; Booton *et al.*, 2014). For SSMIS-F16, these anomalies were mitigated through ground processing (Kunkee *et al.*, 2008; Kroodsma *et al.*, 2021; Swadley *et al.*, 2010) and for F17, changes were made to the

design to address the warm load solar intrusions (Kroodsma *et al.*, 2021). For F18, the reflector antenna was replaced with one which had a higher conductivity to bring it closer to being perfectly reflective (Kroodsma *et al.*, 2021).

2.1.2 First assimilation trials with SSMIS-F18 window channels

The first test undertaken to determine the suitability of including the SSMIS-F18 imager channels (Table 2) into the ECMWF-IFS involved adding all available data for these channels over oceans using the same observational errors used for F17 with no alterations to the Variational Bias Correction (VarBC) settings (Dee, 2004) for SSMIS.

The model used to describe the observational errors associated with the window channels is a piecewise linear model in which the error increases as a function of cloud; cloudy situations are expected to have larger errors due to both the accuracy of the model and observation operator as well as the dynamic range of TBs in these areas (Geer and Bauer, 2010). Figure 1 shows the error model for F17 and F18 and the standard deviation of the BG departures (σ_{BG}) (solid lines) post inclusion of the SSMIS-F18 window channels. These are expected to be similar if the error model is correct. The figure shows that the error model implemented for F17 is reasonably cautious, giving larger observation errors than the standard deviation of the departures. However, given the similarity of the results, it is equally applicable to F18 and, therefore, no changes will be made to the error model for use with F18.

Note that, following convention set out in previous studies (e.g. Geer *et al.*, 2009a,b), the BG departures presented here are bias-corrected, as shown by Eq. 1 where BG_{depar} is the BG departures, $TB_{obs/sim}$ is the TBs of the observations / simulations and b is the bias correction. This removal of the bulk observation-model biases allows for the smaller scale, residual biases to be studied here (i.e. cloud mislocation, observation operator errors and so on).

$$BG_{depar} = TB_{obs} - TB_{sim} - b \tag{1}$$

Note that where simulated TBs are calculated and shown within this work, these are "bias-corrected" to allow direct comparison to the observations, as per Eq. 2.

$$TB_{sim} = TB_{obs} - BG_{depar} \tag{2}$$

For SSMIS-F18, all the channels listed in Table 2 are actively assimilated over oceans only (where the land fraction is less than 1 %) with the same quality control used over ocean for SSMIS-F17. This includes a latitudinal cut-off at $\pm$ 60 degrees, and any sea ice is excluded (using a sea-ice threshold of 0 %) as are locations where the skin temperature is less than 274 K. For SSMIS-F17, the 37.0v GHz and 91.655v GHz channels were assimilated over land as well as ocean (Geer *et al.*, 2022), however, to achieve this, the associated errors relied on the availability of the 150 GHz H (Ch. 8) channel to calculate the scattering index, which failed on-board SSMIS-F18 in February 2012, hence these channels cannot be used over land for F18.

In terms of the number of observations contributing to the active assimilation, it is almost identical for SSMIS-F17 and F18 (i.e. adding F18 doubles the number of SSMIS observations used) with the exception of the 37.0v GHz and 91.655v GHz channels as the observations over land are not used from F18.

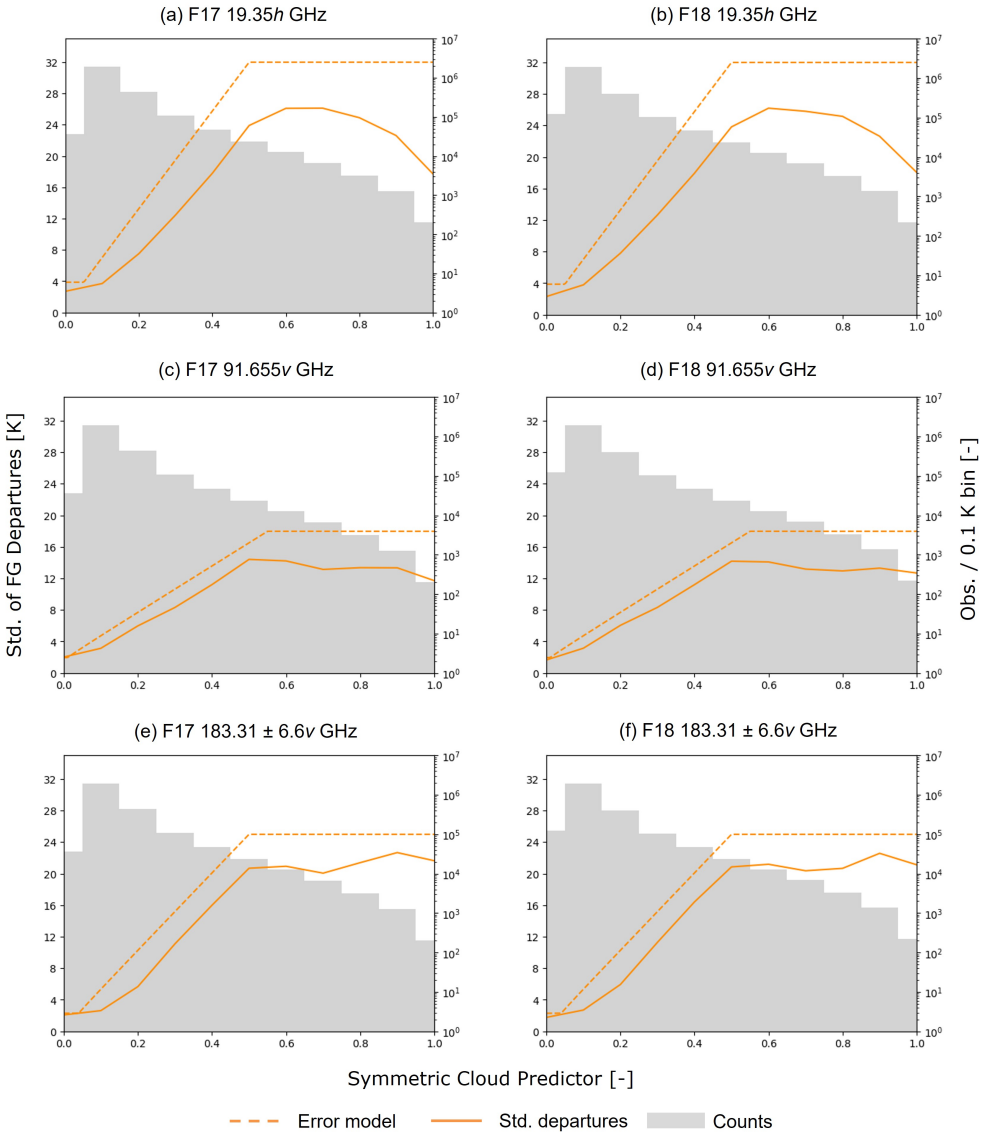

Figure 1: The error model (dashed line) associated with SSMIS F17 (left - a, c and e) and F18 (right - b, d and f) compared to the standard deviation of BG departures (solid line) for the 19.35h GHz channel (a and b), the 91.655v GHz channel (c and d) and the 183.31±6.6h GHz channel (e and f). Counts are shown in gray. Global statistics, for the period 2020-07-01 to 2020-07-31.

Figure 2 shows the relative change in the standard deviation of the BG departures for each microwave imager. Note, for SSMIS, this is the change between the standard deviation of the BG departures for F17 versus those for F17 and F18. In most cases, adding SSMIS-F18 resulted in a positive impact as it reduced the standard deviation of the BG departures for most microwave imager channels on each sensor (i.e. MWRI, GPM Microwave Imager (GMI) and Advanced Microwave Scanning Radiometer 2 (AMSR2)) (see the black line for each panel in Figure 2). This positive impact is also seen in other, independent observations, such as the geostationary satellite instruments with the Himawari and Meteosat water vapour channels seeing statistically significant improvements in the standard deviation of the BG departures of around 0.2 % and the Atmospheric Motion Vectors (AMVs) seeing a similar level of im-

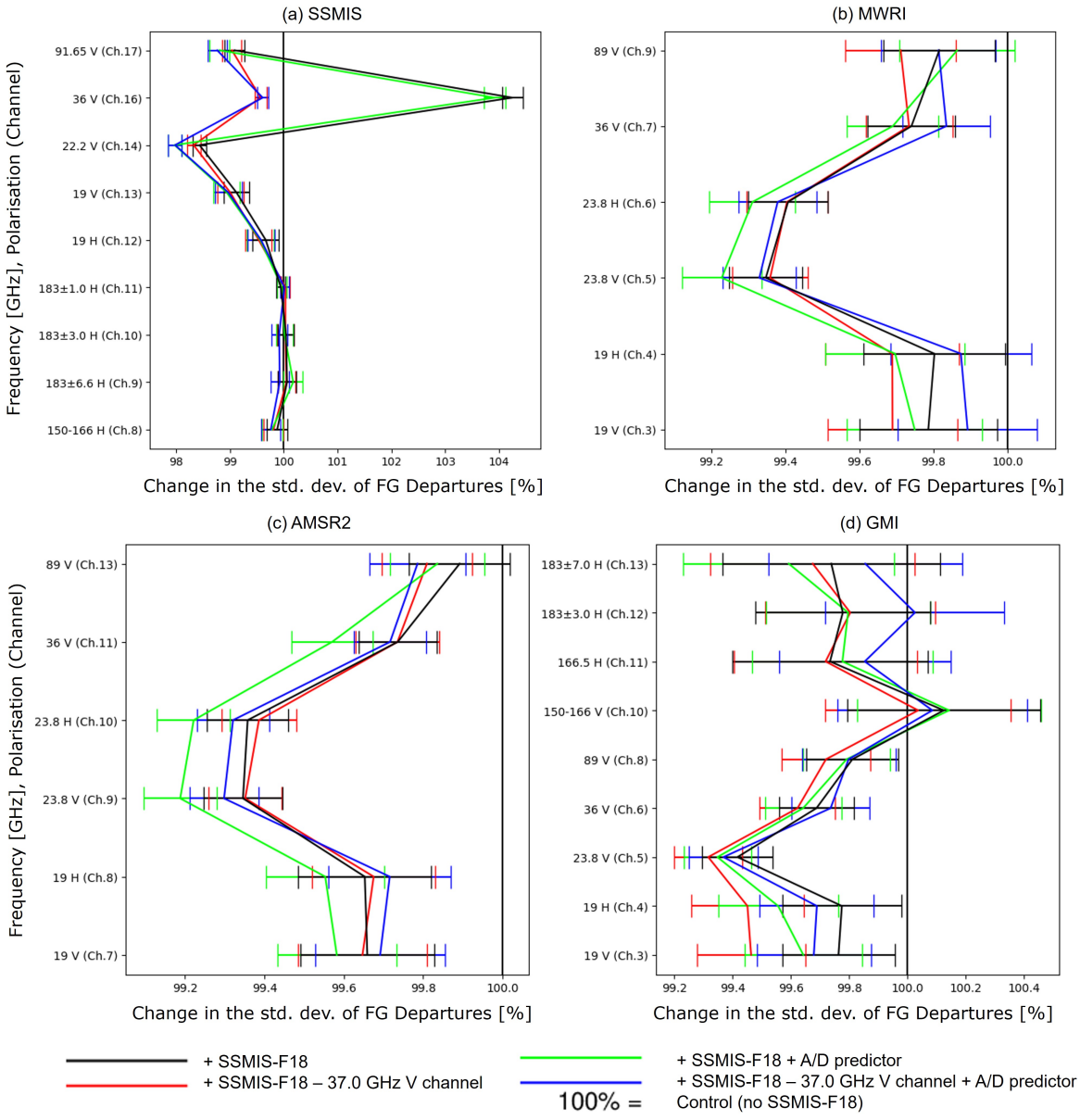

Figure 2: Normalised change in the standard deviation of BG departures for the microwave imagers (a) SSMIS, (b) AMSR2, (c) GMI and (d) MWRI between the control experiment where SSMIS-F18 is not included and various configurations where it is included. Global statistics, for the period 2020-06-07 to 2020-08-31 and 2020-12-07 to 2021-02-28.

provement at the surface (shown in Figure 3). These results provide confidence that the introduction of SSMIS-F18 is benefiting the system as a whole.

However, as we can see in Figure 2(a), the introduction of SSMIS-F18 results in an increase in the standard deviation of BG departures for the SSMIS 37.0v GHz channel of around 4 % when that channel is included (both the black and green lines). In addition to the increase in the standard deviation of the BG departures for the 37.0v GHz channel, it also appears that the inclusion of SSMIS-F18 results in the degradation in the forecast scores (when using both own-analysis and operational verification - see Figures 4 and 5). This particularly affects Relative Humidity (R) and Temperature (T) at surface level

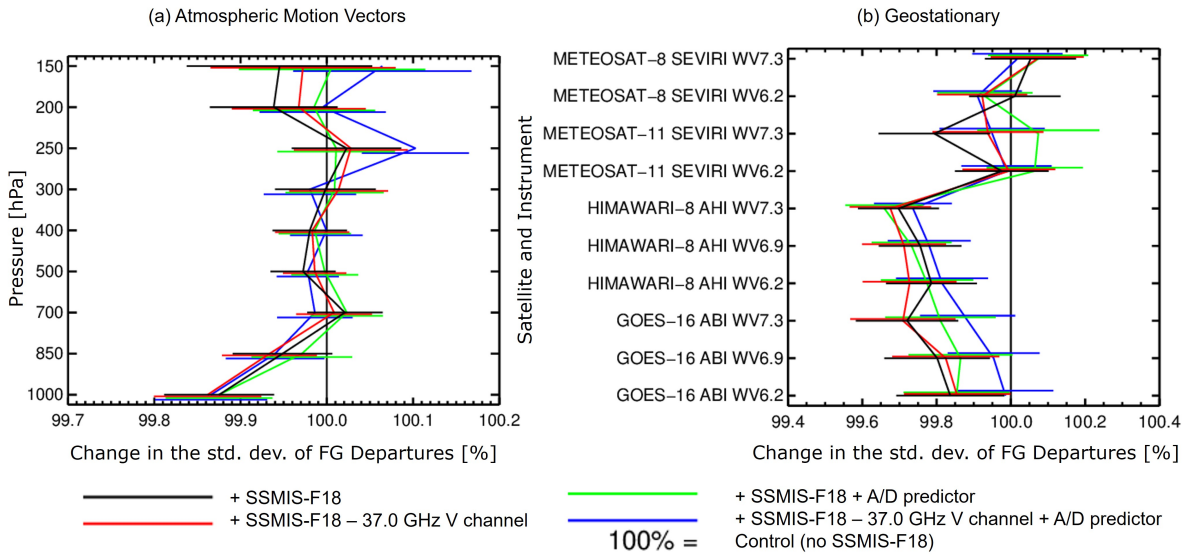

Figure 3: Normalised change in the standard deviation of BG departures for (a) AMVs, (b) geostationary satellites between the control experiment where SSMIS-F18 is not included and various configurations where it is included. Global statistics, for the period 2020-06-07 to 2020-08-31 and 2020-12-07 to 2021-02-28.

(1000 hPa) for the Root Mean Square Error (RMSE) (shown for the RMSE of T in Figures 4 and 5).

Note that there is a large difference in the magnitude and geographical extent of the degradation of the forecast scores due to the inclusion of SSMIS-F18 between the own-analysis and operational verification (Figures 4 and 5). The reduced degradation seen in the operational verification (Figure 5) is a well-known effect that is discussed later on.

2.1.3 Ascending / Descending Biases in SSMIS-F17 and F18

Taking the results of the previous section into account, and the fact there have been discrepancies in the radiometric calibration of SSMIS sensors in the past, it was decided to further investigate the variations in the BG departures with respect to ascending / descending overpasses of SSMIS-F18.

Statistics for the normalised departures[1] for each SSMIS channel are shown in Figure 6 for F17 and F18 split by the ascending and descending nodes, and by season, for the experiments where F18 is actively assimilated. The normalised departures are similar between F17 and F18 for the JJA months, with those of F18 (yellow) being slightly less than those of F17 (red). However, in the DJF months, while F17 (blue) displays similar behaviour to the JJA months, F18 (cyan) shows a rather large deviation especially in the 37.0*v* GHz channel (Ch. 16). In terms of TBs, the mean difference between the ascending and descending node of F18 37.0*v* GHz channel is approximately 1.85 K (descending is warmer).

It is suspected that there is a link between these ascending / descending biases and the degradation seen in the forecast in the Southern oceans (see Figure 4(a) and 5(a)), as both of these effects are much stronger

[1]These are the departures normalised by the final observation error. They are used here as they provide a better indication of the instrument characteristics which would otherwise be dominated by the impact of the cloud and precipitation model errors from the all-sky DA framework.

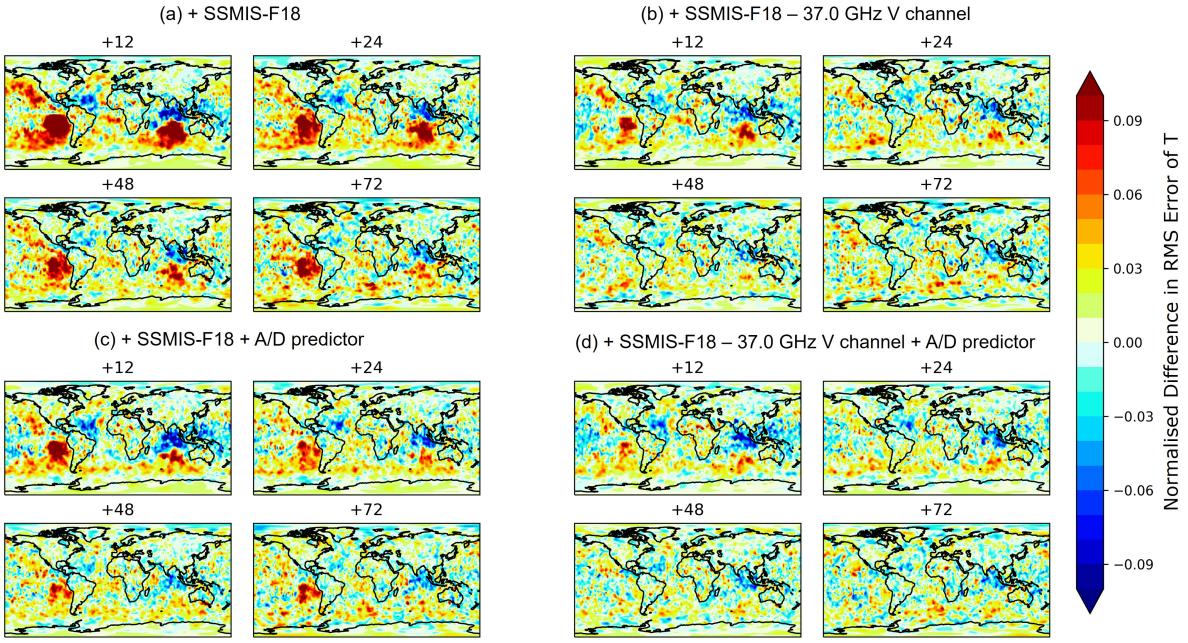

Figure 4: Normalised change in the RMSE of 1000 hPa T forecasts between the control experiment (no SSMIS-F18) and (a) SSMIS-F18 being added, (b) SSMIS-F18 added without the 37.0*v* GHz channel, (c) SSMIS-F18 added using the A/D bias predictor on both SSMIS-F17 and F18 and (d) a combination of (b) and (c), i.e. SSMIS included without 37.0*v* GHz channel and the A/D predictor used. Global statistics, for the period 2020-06-07 to 2020-08-31 and 2020-12-07 to 2021-02-28. Own-analysis verification.

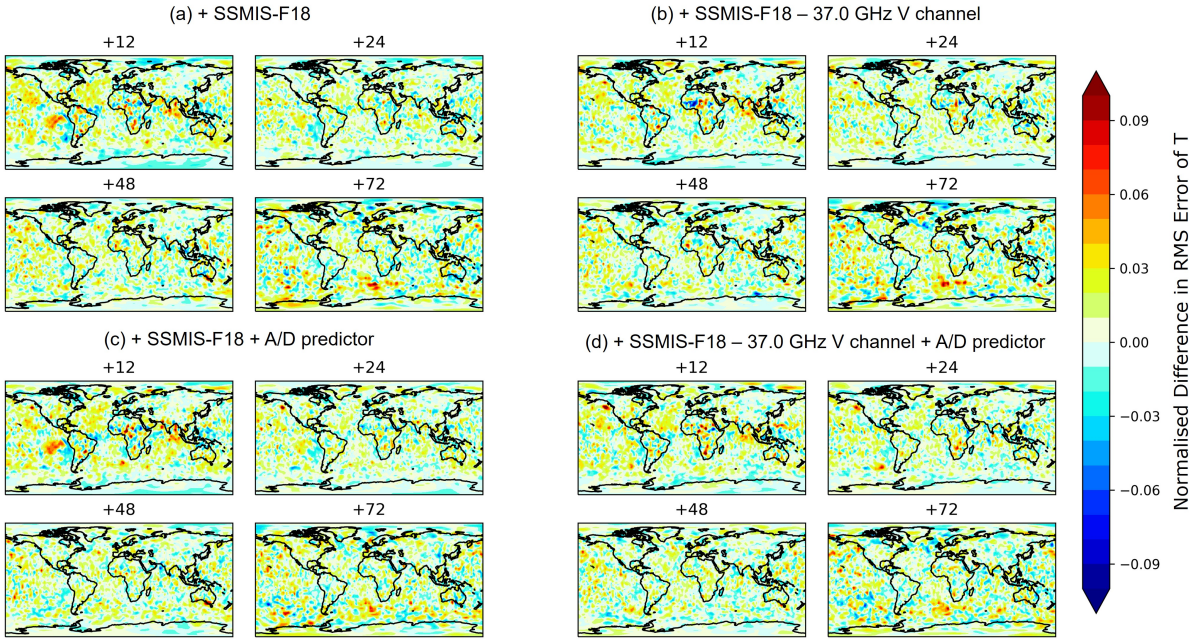

Figure 5: As Figure 4 except operational verification is used.

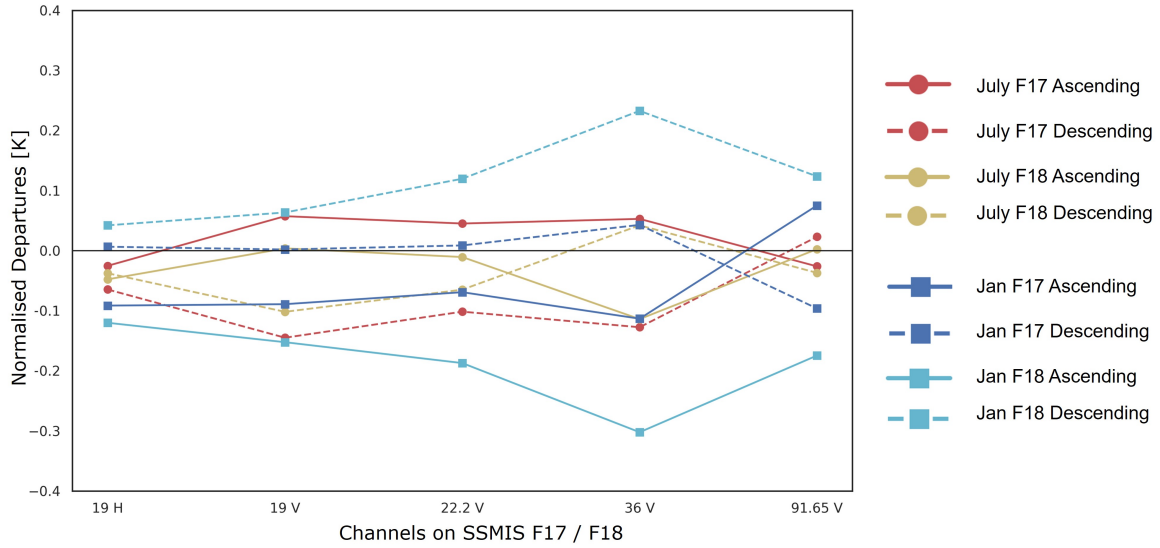

Figure 6: Means of normalised departures for SSMIS channels on-board F17 and F18 split by ascending and descending nodes. Note that for clarity, the standard deviations of the normalised departures are not shown here; these are of the order of 0.7 K to 0.9 K. Global statistics, for the period 2020-07-01 to 2020-07-31 and 2021-01-01 to 2021-01-31.

in DJF. To test this hypothesis, an experiment was run which applied an Ascending / Descending (A/D) bias predictor to the SSMIS data to determine if this could reduce these differences in forecast scores. This predictor works as part of the adaptive bias correction implemented at ECMWF which allows for biases to be characterised by global parameters which are adjusted throughout the Data Assimilation (DA) process (Dee, 2004).

The A/D bias predictor used here is a function of the local solar time that was first introduced at ECMWF to address a 3 K, 46-day period bias observed in the TRMM Microwave Imager (TMI) instrument on-board the Tropical Rainfall Measuring Mission (TRMM); the details of the bias correction method and implementation are presented in Geer *et al.* (2010a). TRMM was placed in a inclined orbit in order to sample all local solar times, and its bias correction is a complex function of these. In contrast SSMIS-F17 and F18 are in polar orbits, meaning that outside the polar regions they only sample two narow bands of local solar times. Hence the Tropical Rainfall Measuring Mission (TRMM) bias predictor is being used here to provide a two-point A/D correction and the additional functional structure targeting TRMM is irrelevant. The re-use of the TRMM predictor is a technical choice made because a special-purpose A/D predictor was not available.

In the current configuration of the ECMWF-IFS, the A/D predictor can only be applied on the sensor level, not to sensors on-board individual platforms. Note that an experiment was run with the A/D predictor turned on for F17 without F18 activated which showed neutral changes in both the fits to observations and the forecast scores. Note, this experiment is is not used as the reference here and instead, the results are directly compared to an experiment mimicking the operational configuration (i.e. no SSMIS-F18).

The green lines in Figure 2 and Figures 4/5(c) show the impact of the use of the A/D predictor when introducing SSMIS-F18. The standard deviation of the BG departures are reduced due to the inclusion of the F18 imager channels. In addition, the degradation in the RMSE of T is significantly reduced when using own-analysis verification, however, when using operational verification, the reduction in

degradation is minimal.

Therefore, it was considered if the forecast score degradation can be further mitigated through the removal of the 37.0*v* GHz channel. An experiment was run with this channel removed (red line in Figure 2 and Figure 4/5(b)) and another with this channel removed and the A/D predictor applied (blue line in Figure 2 and Figure 4/5(d)).

Not including the 37.0*v* GHz channel for SSMIS-F18 results in a reduction (over the case where it is included) of the standard deviation of the BG departures for all MW imager channels with the exception of one GMI channel (red versus black lines in Figure 2). There is little difference in the reduction of the standard deviation of BG departures when the A/D predictor is applied on top of the removal of the 37.0*v* GHz channel (blue lines in Figure 2), and in the case of MWRI, there is an increase in the standard deviation for the 19 GHz channels. However, when we consider the forecast scores (Figure 4/5, panels (b) and (d)), we see that the degradation in the RMSE of R is reduced when the 37.0*v* GHz channel is removed, and even further reduced when the A/D predictor is applied on top of the exclusion of this channel (for own-analysis verification, shown in Figure 4(d)). All experiments show some apparent improvements in the own-analysis verification, primarily in the Indian ocean and eastern equatorial Pacific, so the beneficial impact of F18 imager channels is being retained despite the removal of the 37v channel and the changes to VarBC. With these changes in place, it is expected that the introduction of SSMIS-F18 will positively impact the ECMWF-IFS.

2.1.4 Sensitivity to SSMIS-F17

As discussed in Section 2.1.2, it is expected that SSMIS-F17 and F18 provide complementary information (due to orbital drift resulting in a separation of their equatorial crossing times by nearly two hours). To test the impact of this relatively independent information a sensitivity experiment has been conducted to determine the impact of including F17 (with the A/D predictor) and F18 (with the A/D predictor and excluding channel 16) separately to one another and comparing them against the case where imaging channels from both satellites are excluded. Note that these experiments affect only the imaging channels (Table 2) and not the humidity sounding channel usage of SSMIS, which remains unaffected.

We see that the inclusion of both sensors (F17 and F18) into the system results in an improvement in the fit of the model to independent observations (shown in Figure 7 for geostationary satellites and the IR-imager, Cross-track Infrared Sounder (CrIS)). For both instruments, it is shown that F18 improves the fit the least, followed by F17 (likely due to the use of observations over land from this sensor and the use of the 37.0*v* GHz channel) and finally a combination of both sensors provides the most benefit.

In terms of the forecast scores, we see that the introduction of either or both of the SSMIS instruments results in a slight degradation when using own-analysis verification (see Figure 8). The apparent degradation in R and T in the Southern Hemisphere (SH) for pressures between 700 and 1000 hPa is a well-known effect of adding all-sky microwave imager observations in the ECMWF-IFS and is linked to the fact that at short range, own-analysis verification effectively measures the change in the size of the analysis increments (e.g. Geer and Bauer, 2010).

Note that, while the apparent degradations become less prominent or are absent when using operational verification (not shown), the use of operational verification in this case is complicated to interpret because operational assimilation already includes SSMIS-F17 and therefore it could favour a configuration where an SSMIS-like sensor is included (as demonstrated for a different observing system in Bormann *et al.* (2019)). More broadly, the interpretation of analysis-based forecast verification is always difficult at short range. Many things, other than pure changes in forecast skill, can affect the RMSE. Particularly

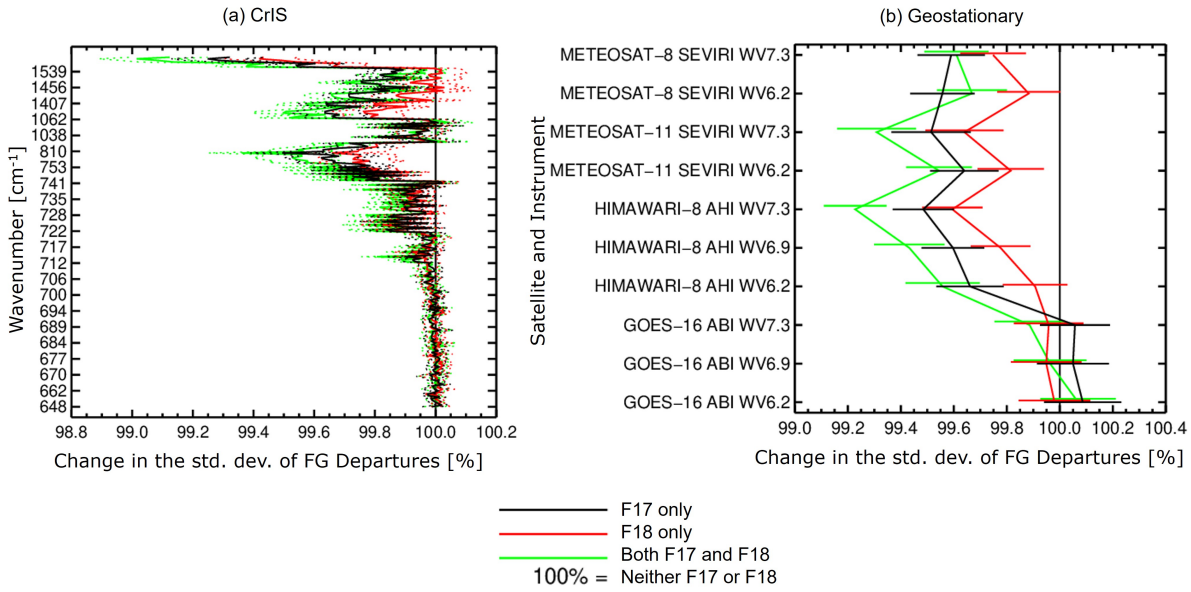

Figure 7: Normalised change in the standard deviation of BG departures for the (a) CrIS and (b) the geostationary satellites when including the imaging channels from either SSMIS-F17 or -F18 or both SSMIS sensors in the observation system. Global statistics, for the period 2020-06-07 to 2020-08-31 and 2020-12-07 to 2021-02-28.

relevant to microwave imagers is the competition between the correlation effect (for example the presence of persistent features observed by microwave imagers that would cause increased correlations between analysis and forecast) and the random effect (transient and semi-random adjustments in the forecast fields made to better fit transient cloud and humidity features). For further information on the choice of reference in verification, see ECMWF (2022) and Bormann *et al.* (2019).

2.1.5 Inclusion within the ECMWF Operational IFS

With the configuration discussed above (A/D predictor and not including the 37.0*v* GHz channel), the use of SSMIS-F18 results in an overall positive impact on the ECMWF-IFS observing system. The inclusion of the data not only reduces the standard deviation of the BG departures in many cases, but, with this particular configuration, also results in the improvement of forecast scores in some areas. It is worth noting that each of these configuration changes (A/D predictor versus not including the 37.0*v* GHz channel) provides different benefits and therefore, it is recommended that the data be activated within the operational ECMWF-IFS using the configuration which includes both changes.

However, it should be noted that the reasons behind the apparent A/D biases associated with SSMIS-F18 are not known. As with all sensors, its performance will be actively monitored within the operational system and should there be any further changes associated with these biases, the use of the data would be reconsidered. Conversely, to allow further exploitation of the sensor, some further investigations could be undertaken.

The main investigation which may yield some positive results not only for SSMIS but also other microwave sensors would be the consideration of alternative A/D predictors. The current TMI based predictor has performed well in this case, however, others could be investigated, for example, the Fourier

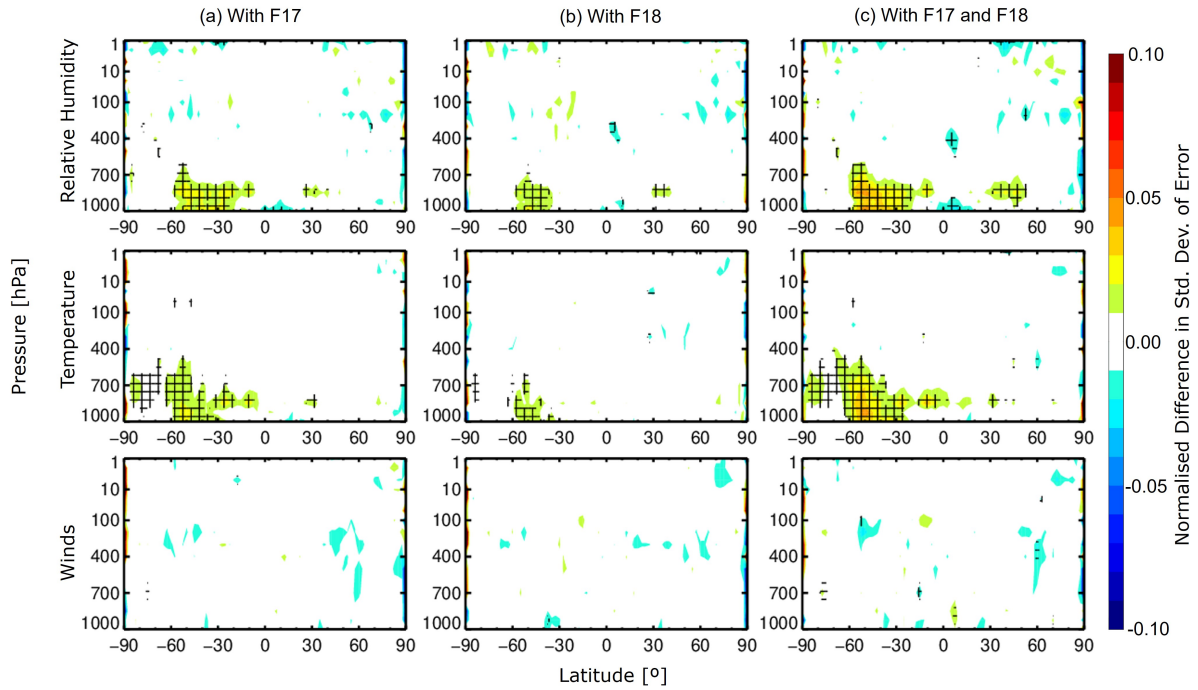

Figure 8: Normalised change in the standard deviation of the forecast error at T+24: relative humidity (top), temperature (middle) and winds (bottom) for experiments where the imaging channels are included from (a, left) SSMIS-F17, (b, middle) F18 and (c, right) both F17 and F18, compared against the case where imaging channels from neither sensor are included. Hatching shows where the results are statistically significant at 95% confidence. Global statistics, for the period 2020-06-07 to 2020-08-31 and 2020-12-07 to 2021-02-28. Own-analysis verification.

series bias correction method tested by Booton *et al.* (2014) was shown to be effective in mitigating the orbital biases associated with SSMIS. Alternatively, improvements could be made to the TMI-based A/D predictor, for example, in the original work Geer *et al.* (2010a) suggested that the use of satellite rather than observation location would be beneficial when considering data around the polar regions.

In addition, the reasons as to why we see such large departures in the 37.0*v* GHz channel particularly in DJF should be further investigated. While not including this channel has been sufficient to allow the other channels to be included into the ECMWF-IFS, knowing why this channel behaves differently to the others would aid in further understanding the orbital biases and perhaps determine if the differences seen between F18 and F17 are an ongoing manifestation of the solar intrusions seen on earlier platforms.

2.2 Removal of MWRI from Operations

2.2.1 Orbital Biases in MWRI

MWRI on-board FY-3D is a conical scanning radiometer with 10 channels between 10 and 90 GHz (WMO, 2022a). Data from the 18.7 *v/h*, 23.8*v/h*, 36.5*v* and 89*v* GHz channels were operationally included in the ECMWF-IFS from May 2020 onwards. However, in January 2021, MWRI started to exhibit some biases between the ascending and descending nodes in terms of normalised BG departures. These biases can be clearly seen to exhibit a sinusoidal pattern in the ascending node dependent on the time of

year (see Figure 9). In October 2021, the difference in the magnitude of the normalised BG departures became much larger (more negative for the ascending node and more positive for the descending node).

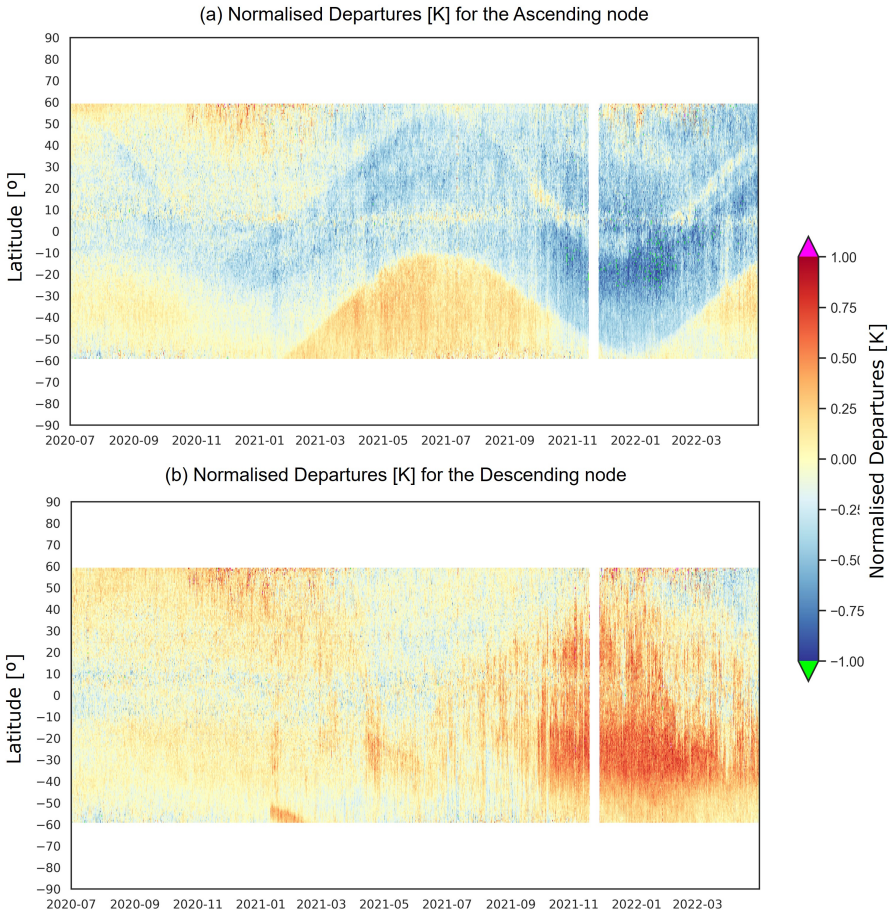

Figure 9: Normalised departures for the ascending and descending nodes of the MWRI 18.7*v* GHz (Ch. 3) aggregated per latitude / cycle. Global statistics, for the period 2020-07-01 to 2022-04-30.

To investigate the impact that these orbital biases were having on the operational system, an experiment in which MWRI was excluded was run. In general, the removal of MWRI resulted in a neutral impact in terms of the standard deviation of BG departures, with minor degradation in some channels, which were rarely statistically significant. However, in terms of the impact on the forecast scores, the removal of MWRI resulted in a positive impact (i.e. an error reduction) in terms of the RMSE of R and T (see Figure 10), particularly in the southern oceans (using operational verification).

This improvement is apparent when using both own-analysis verification and when verifying against operations (the case shown in Figure 10). It is thought that operational verification will favour the control when part of the observing system is being removed as the operational forecast used for the verification includes the removed sensor (e.g. Bormann *et al.*, 2019). Compared to the operational verification, the own-analysis verification shows much larger improvements in the forecast when removing MWRI. However, these may just be apparent improvements, given that own-analysis verification measures the change in analysis increments. Hence the operational verification is favoured here as it likely represents a lower-bound of any potential improvements, therefore, it suggests that removing MWRI improves the forecast.

This positive impact in the forecast scores, along with the large differences in the normalised BG departures between the ascending and descending nodes over time and their clear sinusoidal pattern was enough evidence to warrant the removal of MWRI from active assimilation in the ECMWF-IFS which was implemented on 2022-05-04.

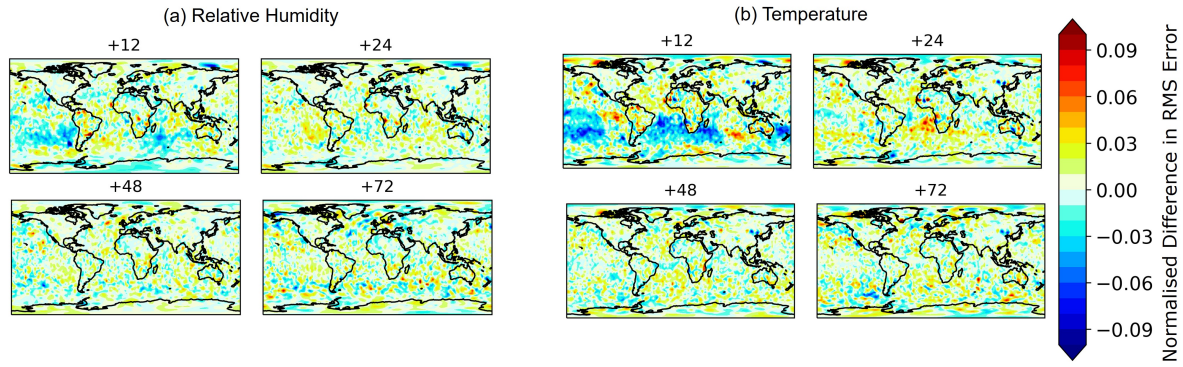

Figure 10: Change in the RMSE of (a) relative humidity and (b) temperature at 1000 hPa for the 12 to 72 hour forecasts due to the removal of MWRI. Blue represents a reduction in the RMSE, hence an improvement. Global statistics, for the period 2021-12-07 to 2021-02-28. Verified against operations.

2.2.2 *Correction Applied by CMA*

The China Meteorological Administration (CMA) found that the difference in the ascending and descending node biases in MWRI was likely due to hot load reflector anomalies. Hence they implemented a correction to the instrument processing in early June 2022. To test the impact of MWRI with this implemented correction, experiments with and without MWRI actively assimilated were run for the period 2022-06-08 to 2023-02-28.

From these experiments, we first evaluate the impact of the correction on the background departures. Figure 11 shows the average normalised departures per 5 degree latitude bin for two different months. The AD bias (the difference between the bias in the ascending (blue) and descending (red) nodes) can be seen most clearly in the northern hemisphere, but it is clearly present for dates both before (solid lines), and after (dashed lines) the correction was applied by CMA. While the bulk bias remains, the correction does appear to have removed some of the zonal structure that was present before: for example, before the correction, a near step-function is present in the ascending bias around 15 degrees S (panel a, July) and 30 S (panel b, September) - this is much reduced in the corrected data.

Figure 12 shows the time-latitude plot (equivalent to Figure 9) for the experiment where MWRI is assimilated post the correction being implemented by CMA. In addition to Figure 11, this confirms that the sinusoidal pattern previously seen has been mostly eliminated with the application of the CMA correction, but there is still a clear seasonal pattern to the biases. In terms of the analysis-based forecast scores, adding MWRI now has an overall neutral impact (not shown). This is different to the situation before CMA implemented the correction, when the result of removing MWRI shown in Figure 10 was to improve the forecast scores. Equivalently, adding MWRI would previously have degraded the forecast scores, but now its impact is neutral. In addition, there is some reduction in the standard deviation of the BG departures for independent observations including AMVs and geostationary satellites. The combination of these indicates that the CMA correction is beneficial and that re-activating MWRI could again provide neutral or small beneficial impact.

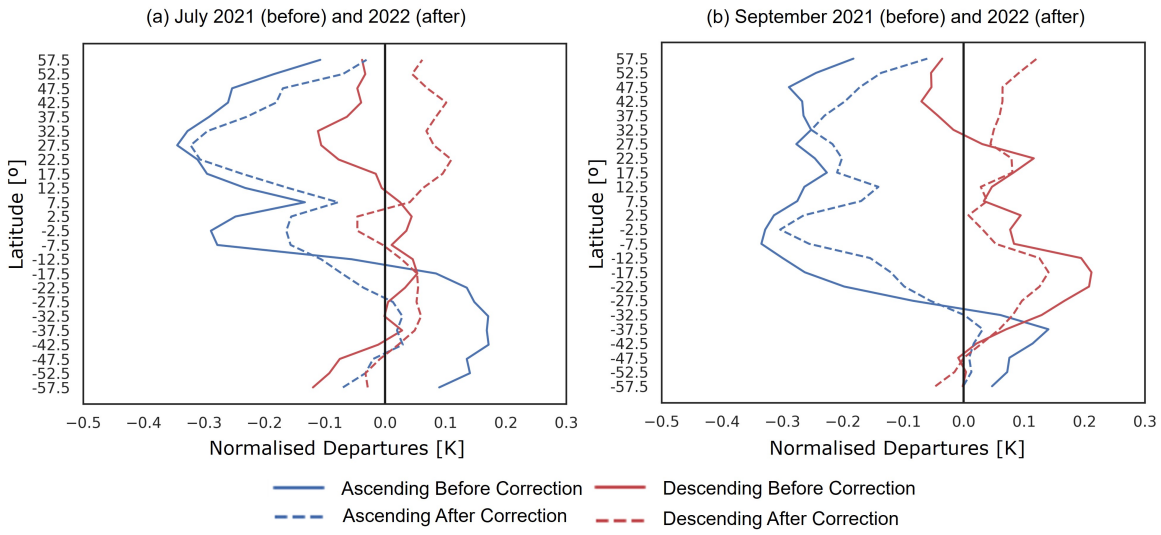

Figure 11: Mean of the normalised departures for before (from 2021) and after (from 2022) the CMA correction is applied for 5 degree latitudinal bins for (a) July and (b) September. Global statistics, for the periods 2021/2-07-01 to 2021/2-07-31 and 2021/2-09-01 to 2021/2-09-30.

However, the biases are not completely addressed through the CMA correction (see Figures 11 and 12) and some latitude and time-dependent features remain. Additional testing using a suitable bias predictor which takes these seasonal changes into account could prove beneficial. Testing is also now in progress (not described here) using an A/D node bias correction for MWRI, which reduces the remaining A/D biases, but cannot address the seasonal latitude-dependent patterns. MWRI will continue to be monitored for the moment and will not yet be reintroduced to the operational ECMWF-IFS, though with further work on bias correction, or further improvements in the CMA processing, there may be a possibility to do so.

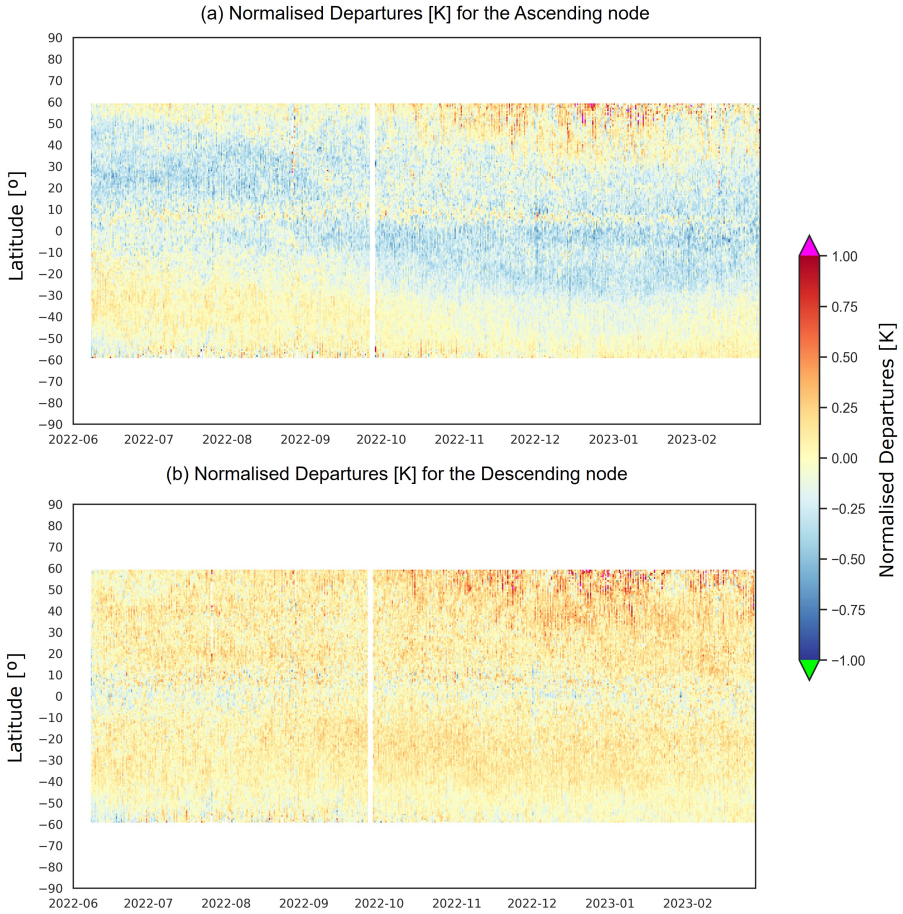

Figure 12: Normalised departures for the ascending and descending nodes of the MWRI 18.7v GHz (Ch. 3) aggregated per latitude / cycle post the application of the CMA correction. Global statistics, for the period 2022-06-08 to 2023-02-28.

2.3 Inclusion of H-Polarisation Channels

Within the ECMWF-IFS, the 37 and 89*h* GHz-polarisation channels have not yet been utilised from any of the currently assimilated MW imagers (see Table 1, which gives the specific frequencies for each sensor). Whilst it is thought that these channels could contain useful information on water vapour and cloud, their inclusion in the current configuration of the ECMWF-IFS observing system has not yet been tested.

This work includes each channel over oceans only and utilising the already available error models (shown in Figure 13). Three configurations are tested: the inclusion of the 37*h* GHz channels for all sensors, the inclusion of the 89*h* GHz channels for all sensors and finally the inclusion of both the 37 and 89*h* GHz channels for all sensors; each of the configurations are run over two seasons (JJA 2020 and DJF 2020/1).

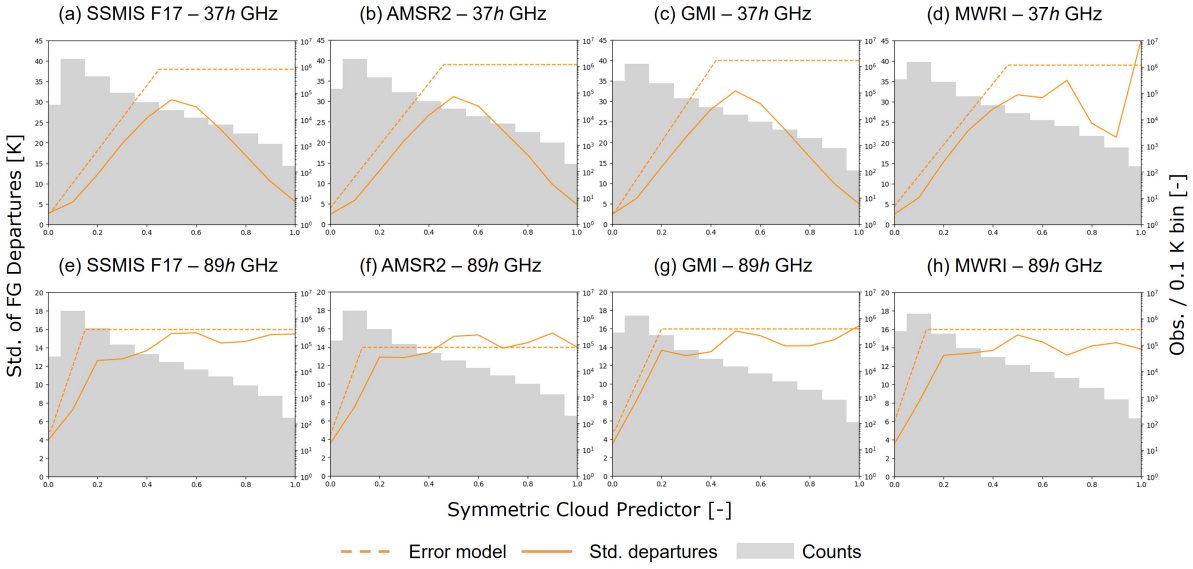

Figure 13: The error model (dashed line) associated with the 37*h* GHz (top) and 89*h* GHz (bottom) channels compared to the standard deviation of BG departures (solid line) with counts shown in grey for all MW imagers. Global statistics, for the period 2020-07-01 to 2020-07-31.

In terms of the fit of the model to the observations (Figure 14), we see a general trend of degradation for all configurations tested (in terms of the standard deviation of the BG departures). In most cases, the degradation is small in magnitude and for some sensors it fluctuates between a very minor improvement and a slightly larger degradation depending on the channel, pressure or wavenumber.

As an example, Figure 14(a) shows a statistically significant increase in the standard deviation of BG departures of AMVs, suggesting a degradation of the quality of the short-range forecast of wind at lower levels. For the geostationary satellite radiances (Figure 14(b)), which also show significant changes in the fit, it appears there is some benefit from including the 37 GHz channel from all sensors by itself, however, this improvement is primarily constrained to the tropics with both the northern and southern hemispheres showing a degradation of the fit for these sensors (split by geographical region not shown).

In terms of the forecast scores (see Figure 15), we see that including these channels in any configuration results in a statistically significant degradation in not just the R and T fields, but also in the winds. The effect on R and T is to some extent expected, but not the degradation in winds (compare to Fig. 8). While the own-analysis verification is shown in Figure 15, statistically significant degradation is still apparent

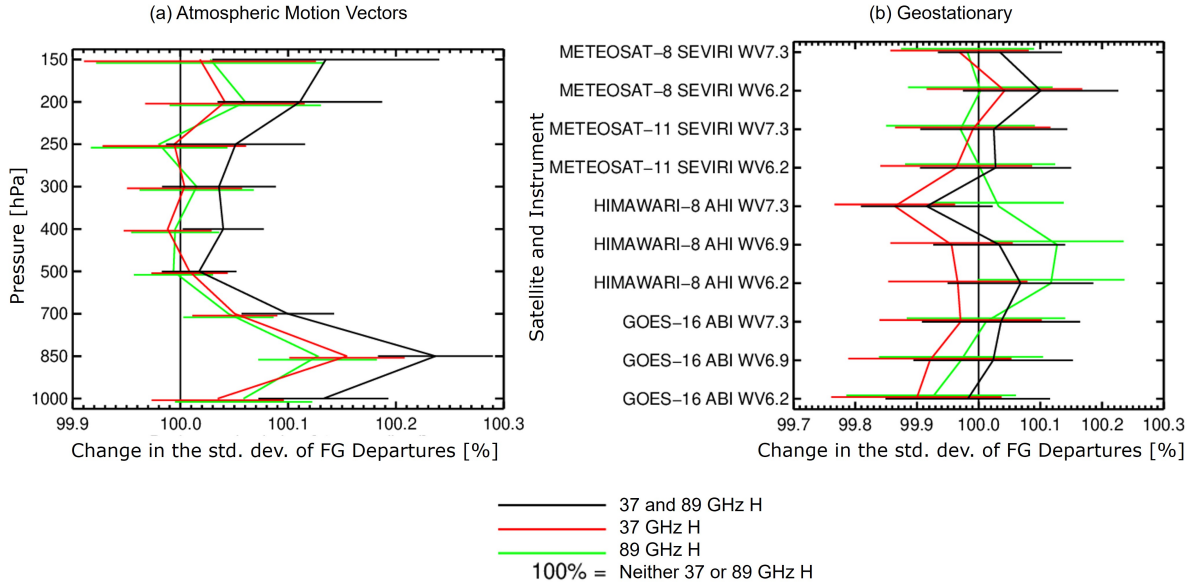

Figure 14: Normalised change in the standard deviation of BG departures for (a) AMVs, (b) geostationary satellites as a result of the inclusion of the H-polarisation channels. Global statistics, for the period 2020-06-07 to 2020-08-31 and 2020-12-07 to 2021-02-28.

in R, T and winds fields when using operational verification (which will favour the control in which these channels are not included).

Taking these results into account, it is clear that to include the 37 GHz and 89h GHz polarisation channels at this time is not beneficial. There may be some ways in which the results can be improved, for example tuning the error models (see Figure 13), taking into account the inter-channel error correlations between the V and H polarisations, testing these channels from each of the sensors individually, or looking for physical explanations for the problem with these H channels (such as the quality of surface emissivity modelling for these frequencies and polarisations).

Without significant further work to address these issues, these channels cannot be actively assimilated in the observing system for the ECMWF-IFS, but note that these channels are still providing benefit in the system, for example by helping to drive the observation error models (e.g. Geer and Bauer, 2010).

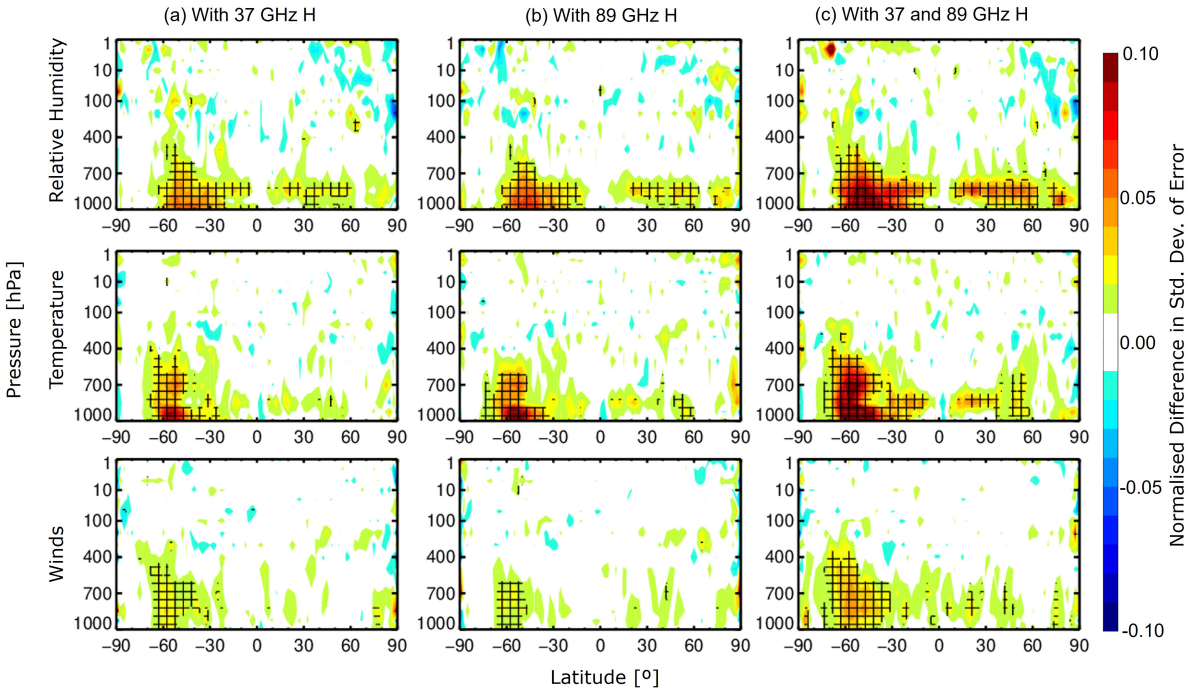

Figure 15: Normalised change in the standard deviation of the forecast error at T+24: relative humidity (top), temperature (middle) and winds (bottom) for experiments where (a, left) the 37*h* GHz channels are included, (b, middle) the 89*h* GHz channels are included and (c, right) both 37*h* and 89*h* GHz channels are included from all microwave imagers (SSMIS, AMSR2, GMI and MWRI) compared against the case where neither of the channels are included. Hatching show the results are statistically significant. Global statistics, for the period 2020-06-07 to 2020-08-31 and 2020-12-07 to 2021-02-28. Own-analysis verification.

3 Representation of Convective Situations

3.1 The ECMWF Cloud Fraction Model

In all-sky assimilation at ECMWF, the simulated TBs are a combination of the clear and cloudy TBs (generated using RTTOV, Saunders *et al.* (2018)) weighted by an effective cloud fraction. To provide accurate simulated TBs, it is important to ensure the cloud fraction used precisely (as far as possible) represents the vertical variability of cloud fraction (Geer *et al.*, 2009a). Currently, the total cloud fraction is a weighted sum of clouds, convective precipitation and large-scale precipitation (see Eq. 3 taken from Eq. 3 of Geer *et al.* (2009b)), each of which have a grid-box fraction associated with them. This weighted approach was introduced to avoid the overestimation of simulated TBs resulting from using the maximum cloud fraction (Geer *et al.*, 2009b).

$$C_{av} = \frac{\sum_i \left((l_i + i_i)C_i + (r_i^c + s_i^c)C^c + (r_i^l + s_i^l)C_i^l\right)\Delta z_i}{\sum_i \left(l_i + i_i + r_i^c + s_i^c + r_i^l + s_i^l\right)\Delta z_i} \tag{3}$$

Where l_i, i_i, r_i^c, s_i^c, r_i^l, s_i^l represent the densities of the different hydrometeor types at each layer i (cloud water, cloud ice, convective rain and snow, large-scale rain and snow, respectively). Δz_i is the layer geometric thickness and C_i, C^c and C_i^l represent cloud, convective precipitation and large scale precipitation fractions at each layer, noting that convective fraction is a constant.

The cloud (C_i) and large scale precipitation (C_i^l) fractions are diagnostics from the model at each level (based on the outputs of the convective and large scale moist physics parameterisations), whereas the convective precipitation (C^c) fraction is not a model diagnostic but an assumption; it is this assumption that is the focus of this work. Within the ECMWF-IFS it is set at a constant 0.05 (5 %) for all levels (Geer *et al.*, 2009b).

The assumption of 5 % convective precipitation at all levels is thought to result in an underestimation of overall cloud fraction (ECMWF, 2017) and it has been questioned if this value is too small to represent intense tropical convection (Geer, 2021). An underestimation of the cloud fraction may result in large BG departures. This would manifest as negative BG departures in regions and channels (high microwave frequencies, e.g. $>$ 90 GHz) where scattering is expected (primarily from snow) and the opposite in regions and channels (low microwave frequencies, e.g. $<$ 90 GHz) where absorption is stronger (primarily from rain). When these extreme values are either large enough in magnitude or number, they can skew the distribution of the BG departures.

The mean and skewness of the BG departures of a control experiment (cloud model not implemented) are shown per 2.5 x 2.5 degree geographical bin[2] over the month of July 2020 in Figure 16 for two SSMIS channels to demonstrate different scattering / absorption regimes. The 19.35h GHz channel (Ch. 12) (left, panels (a) and (c)) shows some positive BG departures (top) and associated positive skew due to the under-estimation of simulated TBs, particularly in the ITCZ and between the Indian sub-continent and the maritime continent. The 183.31$\pm$6.6h GHz channel (Ch. 9) (right, panels (b) and (d)) shows the opposite - negative BG departures and associated skew due to the over-estimation of simulated TBs, in the same areas.

Note that for all panels of Figure 16, all data is included and therefore some of the large and / or noisy BG departure values are resulting from data that is screened out, and subsequently not used, during the

[2]This bin size is used as it results in each data point containing approximately the same number of observations over oceans.

DA process (for example, these areas include the positive departures in the southern ocean especially between South America and Australia, which are removed by cold air outbreak screening).

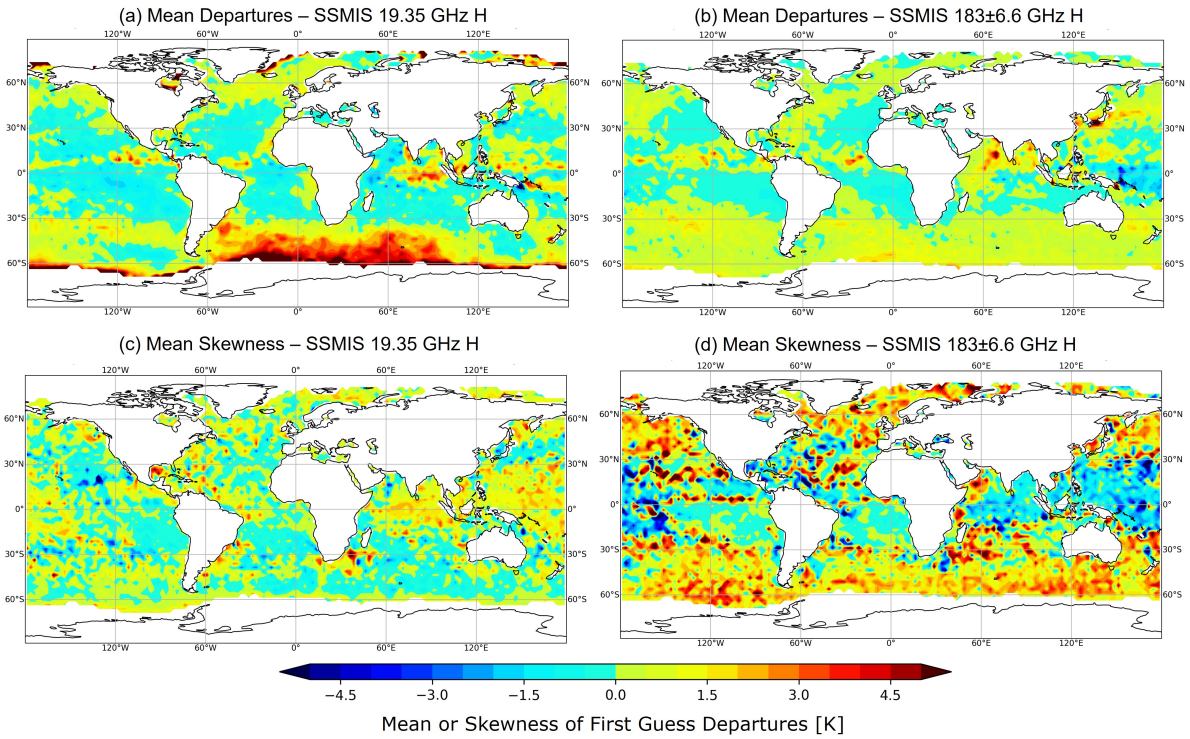

Figure 16: Mean (top) and skewness (bottom) of BG departures binned per 2.5x2.5 degree box. Shown for SSMIS (left) 19.35h GHz and (right) 183.31±6.6h GHz. Global statistics, for the period 2020-07-01 to 2020-07-31.

3.2 A Cloud Fraction Model for Convective Situations

To move away from the 5 % assumption for convective precipitation, a new model has been devised which increases the convective precipitation fraction in the frozen part of the cloud. A linear-in-pressure model has been implemented from the freezing level to the top of the anvil which increases the fraction from 5 % to the maximum cloud fraction available in that grid box. This maximum cloud fraction is taken from the model and is used on the basis that within the ECMWF-IFS, cloud water and ice are detrained into the large-scale scheme. This typically represents anvil clouds as a single vertical layer at the top of the convection with a large cloud fraction ('high and thin' anvils, Geer, 2021) and also means that convective profiles show their highest cloud fraction at the detrainment level. Where the maximum level is below 5 %, the convective precipitation fraction is maintained at 5 % over all levels. The equation for the new convective precipitation fraction model (for each level) is given in Eq. 4 with a visual representation of the model and the associated parameters shown in Figure 17.

$$C_i^C = \begin{cases} \left(\frac{C^m - 0.05}{P^t - P^f}\right)(P_i - P^f) + 0.05 & P^f > P^t, C^m > 0.05 \\ 0.05 & P^f \leq P^t, C^m \leq 0.05 \end{cases} \tag{4}$$

Where C_i^C is the convective precipitation fraction per level, C^m the maximum cloud fraction in that grid

box, P^t the pressure at the top of the anvil cloud, defined at the level (above the freezing level P^f), where the cloud fraction is at its maximum with the model (C^m), P^f is the pressure at the freezing point and P_i is the pressure for the level of interest. This equation is applied at all levels of the model within each grid box where a simulated TB is calculated.

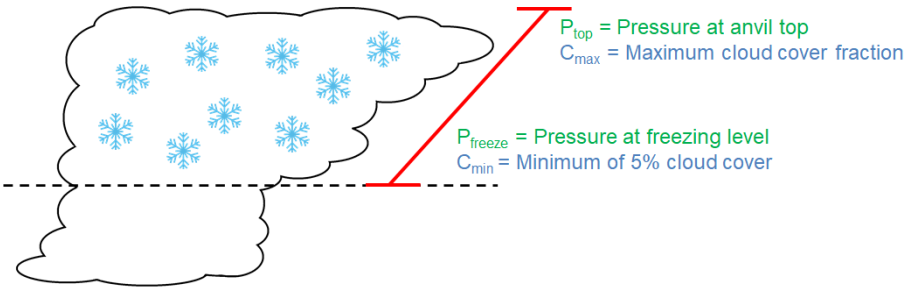

Figure 17: Cloud fraction model showing how the convective fraction in the anvil part of the cloud (frozen only) is modeled under the new scheme.

To test the new model, a passive reinitialisation experiment (DA not undertaken) has been run for two seasons: JJA 2020 and DJF 2020/1. The impact of the new model on the overall cloud fraction averaged for all levels (C_{av} from Eq. 3) is shown for a single cycle in Figure 18. The new model results in a widespread, small magnitude increase (<0.05) to the cloud fraction in the SH temperate zone with isolated high-magnitude increases in the Intertropical Convergence Zone (ITCZ), up to around 0.15. This single cycle is representative of the overall case, as can be seen in the histogram of changes over a month (Figure 18 (b)) which shows a maximum increase of between 0.4 and 0.6 (dependent on month) for a very few points with the majority of changes being much smaller.

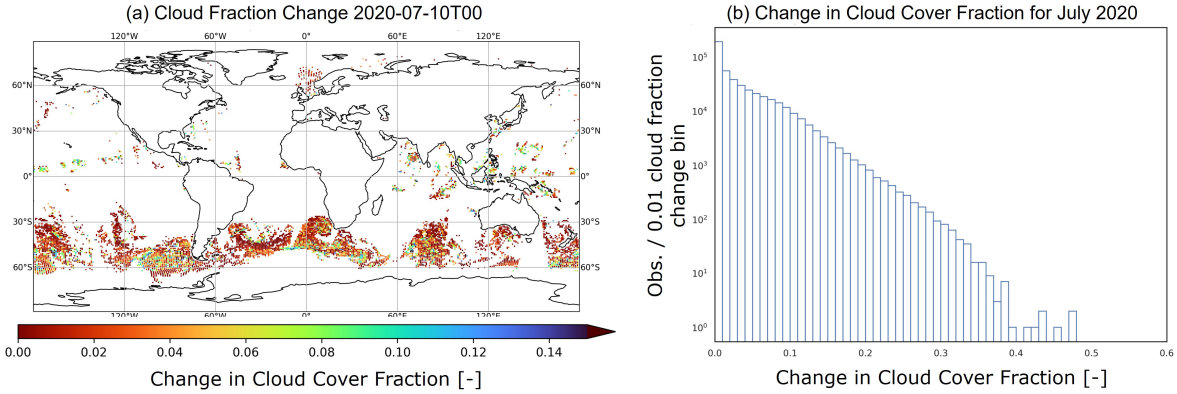

Figure 18: Changes in cloud cover fraction (C_{av} from Eq. 3) for (a) a single cycle and (b) the distribution over a month, due to the implementation of the new convective precipitation fraction model. Global statistics, for (a) 2020-07-10 and (b) the period 2020-07-01 to 2020-07-31.

3.3 Impact on Simulated Brightness Temperatures and BG Departures

The implementation of this model affects all microwave sensors (both imagers and sounders) currently assimilated within the ECMWF-IFS. For brevity, within this report, results from SSMIS are presented as it covers a large range of channels (19 GHz to 183 GHz) with a large geographical extent and some

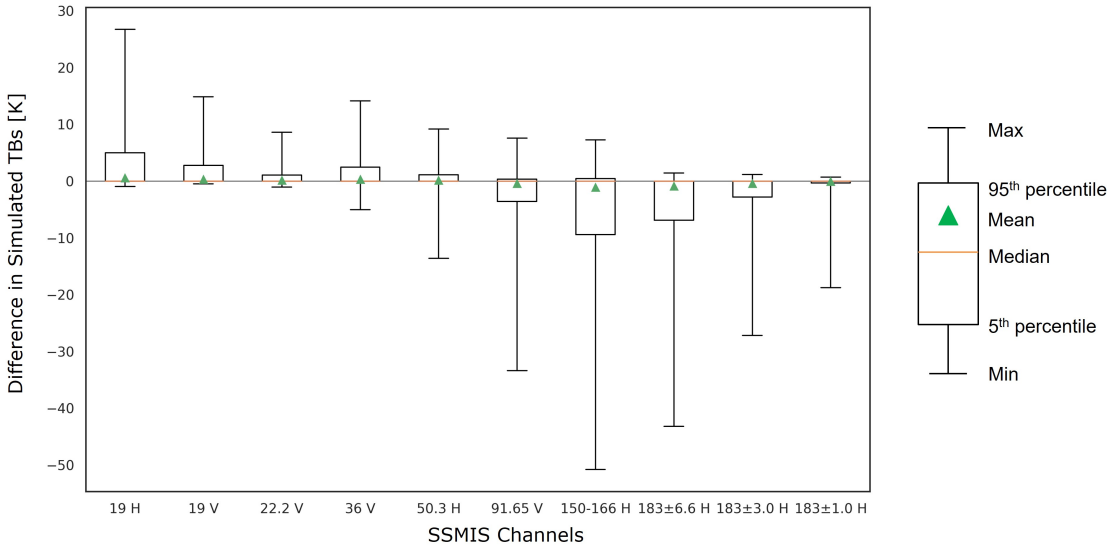

Figure 19: Changes in simulated TBs for SSMIS when the linear convective precipitation model is applied (showing only points which have changed). Global statistics, for the period 2020-07-01 to 2020-07-31.

results from GMI are presented as it is considered the best calibrated microwave sensor (Lean *et al.*, 2017) (although with a reduced spatial extent over SSMIS due to its inclined orbit).

The distribution of changes in the simulated TBs for SSMIS due to the cloud fraction changes is shown for all channels in Figure 19. The magnitude of the mean changes is extremely small (close to 0) for all channels (which is consistent with the results shown in Geer *et al.* (2009b)), however, there are also a few points which make changes of up to +30 K/-50 K in some channels, which is exactly the kind of changes targeted by the new cloud model.

Figure 20 shows the geographical extent of the changes, for observations from a single cycle of the DA, with a restricted colour scale to highlight widespread small changes in brightness in temperature latitudes (typically less than 0.001 K, Figure 20(a)) and a broader colour scale to highlight the much smaller and more localised sample for which there are much larger changes (colour scale up to 20 K, Figure 20(b)). It was expected that the main effects would be confined to the tropical and sub-tropical regions as per the changes made through Geer *et al.* (2009b), and indeed the changes large enough to be visible in Figure 20(b) are mainly in these expected areas. However, as seen in Figure 20(a) as well as Figure 19, there are geographically extensive (but limited magnitude) changes also present in the SH temperate zone where cold sector cumulus clouds and convection embedded in fronts can be found.

Figure 21 shows the distributions of simulated TBs for 2 SSMIS channels separated by Total Column Water Vapour (TCWV) at 25 kg m^{-2} (broadly representing tropical (above) and extra-tropical (below) regions) both before and after the implementation of the convective precipitation fraction model (blue and orange lines), along with the distribution of the related observed TBs (green lines). For the 19.35h GHz channel, the implementation of the convective precipitation model has very little impact on the simulated TBs with only a slight increase around 200 K which brings the simulated TBs closer to the observed TBs. For the 183.31$\pm$6.6h GHz channel, more significant changes can be seen, both above and below the TCWV threshold. In both cases, there are more occurrences of simulated TBs in the range 200 to 250 K, with the largest change being seen in the TCWV $>$ 25 kg m^{-2} case. In the TCWV $<$ 25 kg m^{-2} case,

the implementation of the model results in the distribution of the simulated TBs matching observations slightly better for the 19.35h GHz channel. However, for the 183.31pm6.6h GHz channel, we see a slight improvement below around 215 K but above this (up to 250 K), the distribution of the post-model simulated TBs are further from the observations. The exact reason for this shift is unknown but could be values from the peak TBs (around 270 K) being reduced.

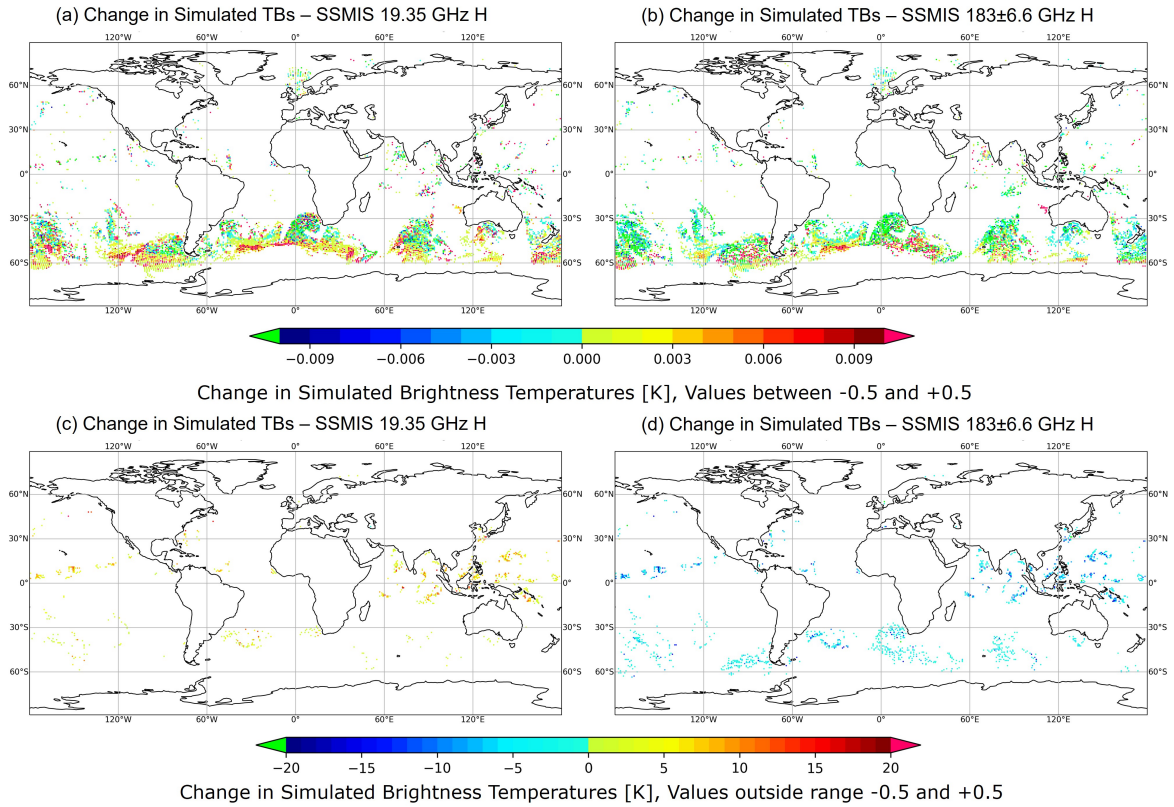

Figure 20: Change in simulated TBs when the linear convective precipitation model is applied for 2020-07-10T00. Panels (a) and (b) (top) show changes between -0.5 and +0.5 and (c) and (d) bottom show changes outside of this range. Shown for SSMIS (left) 19.35h GHz and (right) 183.31±6.6h GHz.

Whilst it is important to see that the simulated TBs are changing (presented in Figures 19, 20 and 21), the key performance metric to consider is the BG departures (with the bias removed, as per Eq. 2), i.e. do the changes in simulated TBs result in a reduction in the difference between the observations and simulated TBs? To evaluate this, we have chosen to look at the skewness of the distributions of the BG departures as these give us an idea of how the most extreme values have changed due to the implementation of the new convective precipitation model.

Figure 22 shows how the skewness has changed (for the month of July 2020) due to the implementation of the new convective precipitation model. Comparing to Figure 16, it can be seen that, in the tropics, the skewness has moved towards zero for both channels shown: for the 19.35h GHz channel the large positive skew has reduced and for the 183.31±6.6h GHz channel the large negative skew has increased. These changes provide confidence that the convective cloud model is resulting in the reduction of outliers in the BG departures. Outside of the tropics, Figure 22 shows that for the 183.31±6.6h GHz the skew becomes larger which may be a result of a lot of points changing by a small magnitude in these areas (as per Figure 20.

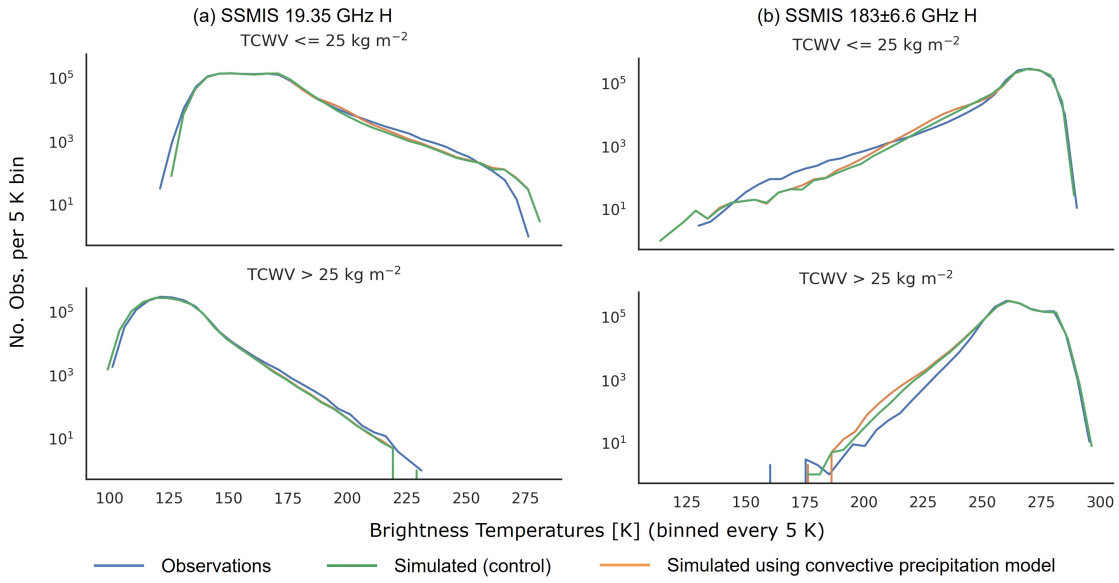

Figure 21: Histograms of observed and simulated (bias corrected) TBs for SSMIS (a) 19.35h GHz and (b) 183.31±6.6h GHz with and without the convective precipitation model applied. Note that a logarithmic scale is used for the y-axis to better visualise the tails of the distribution. Global statistics, for the period 2020-07-01 to 2020-07-31.

Whilst the effect on the outliers can be seen in the skewness of BG departures for SSMIS (Figure 22), the changes in the mean BG departures is harder to discern due to the large mean magnitude of those departures. GMI however, being the best calibrated sensor (Lean *et al.*, 2017), provides a clearer picture. Figure 23 shows the change in the standard deviation (Figure 23(a)) and mean (Figure 23(b)) of BG departures for GMI in the tropics, with the blue line being the control experiment (5 % convective precipitation) and black being the experiment where the linear model is implemented. Note that the red and green lines will be discussed in Section 3.4.

The increase in the standard deviation in scattering channels (89.0 GHz and up) is expected as clouds may have been, on average, intensified in the model simulations to better match the Probability Density Function (PDF) of the observations. Since the clouds are often in different places in the model and observations, the double penalty effect (e.g. Geer, 2021) means that increased standard deviations are to be expected. In emission channels (36.5 GHz and below) we see very minor changes in the standard deviation. For the mean BG departures, we see the scattering channels cooling by a maximum average of 0.1 K and and the emission channels warming by 0.2 K. This particular case demonstrates that, although the changes made are resulting in an increase to the standard deviation of the BG departures, the mean of the BG departures is improving.

3.4 Sensitivity to Minimum Convective Cloud Fraction

As can be seen from Eq. 4, the previous assumption of a minimum convective fraction of 5 % has been retained in this work. Work has already been undertaken to determine the sensitivity of the cloud fraction model to the 5 % convective precipitation fraction and it was shown to have a very small effect on the effective cloud fraction (Geer *et al.*, 2009b, 2017). However, for completeness, a short study has been undertaken here to test the use of a higher minimum convective precipitation fraction (10 %) both with

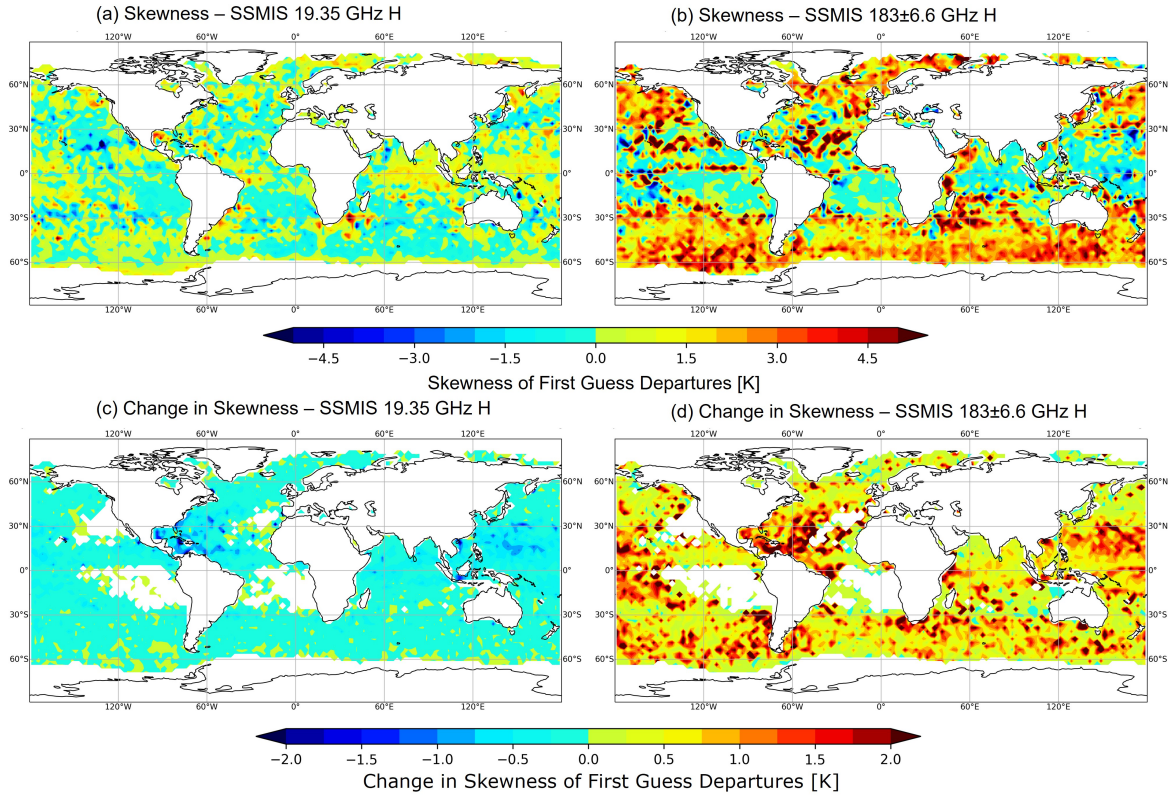

Figure 22: Skewness (top) and change in skewness (bottom) of BG departures as a result of implementing the linear convective precipitation model for 19.35h GHz and (right) 183.31±6.6h GHz. Global statistics, for the period 2020-07-01 to 2020-07-31.

(replacing 0.05 with 0.1 in Eq. 4) and without (making C^C in Eq. 3 equal to 0.1) the linear hydrometeor fraction assumption applied. The results are shown as the red and green lines in Figure 23.

Figure 23 shows that, in terms of the absolute magnitude of the mean BG departures, the linear model with a 5 % convective precipitation minimum (black line) performs best for most channels. While the 10 % minimum with the linear model performs best in terms of the mean for the 18.7h GHz channel, this is the only channel where that is the case. As was found in Geer *et al.* (2017), the use of 10 % (for both the static case and the linear model), results in lower absolute mean BG departures than the 5 % static case. In terms of the standard deviation, there is very little difference between the 5 % (with the model) and 10 % (with or without the model) convective precipitation minimum.

While it is interesting to see that the impact of changing the minimum convective fraction, this work has shown that, with the linear model applied, the best case is using a 5 % minimum with the linear model implemented.

3.5 Inclusion within the ECMWF Operational IFS

The use of the 5 % cloud fraction for convective precipitation has been in place in the ECMWF-IFS since 2009. The associated underestimation of overall cloud fraction has resulted in some localised large negative (high frequencies) and positive (low frequencies) biases between the observations and simulated TBs. The implementation of the cloud fraction model described here has been demonstrated to reduce

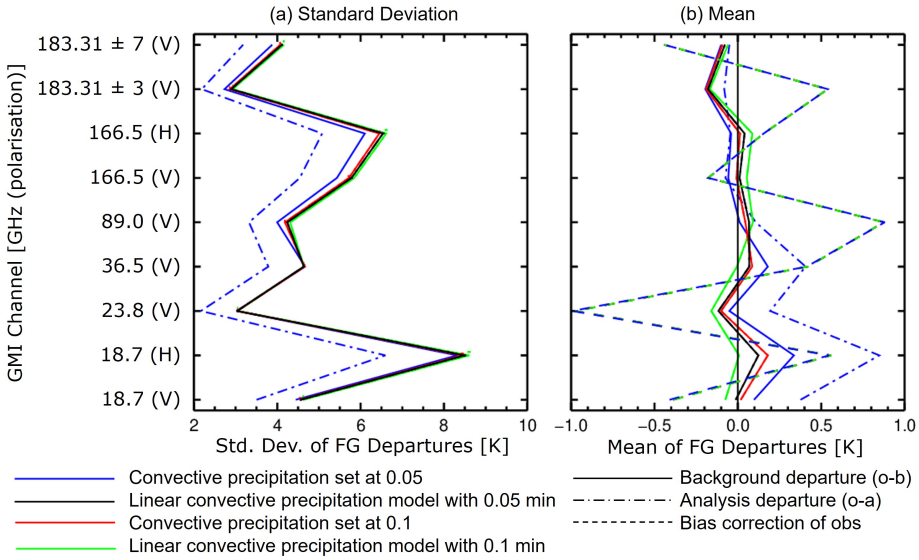

Figure 23: The (a) standard deviation and (b) mean of the BG departures for GMI in the tropics for the case where the convective precipitation fraction is constant at a 5 % or 10 % and where the linear model is applied using either 5 % or 10 % as a minimum cloud fraction. Tropics statistics, for the period 2020-06-07 to 2020-08-31 and 2020-12-07 to 2021-02-28.

these biases in some key areas (namely the ITCZ and in particular over the maritime continent) and it has been shown that the model performs best in terms of BG departures when compared against other configurations.

To determine the suitability of implementing the convective precipitation model in the ECMWF-IFS, a full DA experiment has been run with the convective fraction changes also included in the tangent linear and adjoint models activated (note that up until now, all results presented are from passive monitoring experiments). The results from these experiments show similar changes in the distribution of the simulated brightness temperatures and expected modifications to departure statistics for the MW imagers as highlighted earlier, but neutral impact otherwise in terms of background departures for other observations or forecast scores. Nevertheless, the implementation of this convective cloud fraction model represents a useful step forward in terms of modelling the simulated TBs and reducing errors in the BG departures.

However, there are some potential improvements that could be implemented to further tune the model and hence reduce the large outliers in the BG departures. For example, the use of a limit to the convective precipitation could be considered, as is currently the case for shallow convection (limited between 5 % and 45 %) (ECMWF, 2021). On a larger scale, the recommendation that the average (effective) cloud fraction should be determined per frequency could be revisited (Geer *et al.*, 2009b,a).

Although this small change to the convective precipitation modelling has resulted in some small improvements to the simulated TBs, it should be noted that there is still work to be done to address other errors, for example revisiting the micro-physical assumptions such as Particle Size Distribution (PSD) and particle habit or improvements to the modelling of scattering properties of snow hydrometeors (Geer, 2013) or reconsidering the assumptions made within the overall effective cloud fraction (see Eq. 3).

4 Hydrotable Range Extensions

4.1 Hydrotables in RTTOV-SCATT

The observation operator used in the ECMWF-IFS, RTTOV (Saunders *et al.*, 2018), will be updated at the next ECMWF-IFS version (48r1) to Version 13.0. This new version, described in Geer *et al.* (2021) and (Saunders *et al.*, 2020), actively uses hydrometeor optical properties from the Atmospheric Radiative Transfer Simulator (ARTS) database for the first time and improves some of the micro-physical assumptions used in the generation of the hydrotables (lookup tables for the bulk optical properties of a range of hydrometeors: rain, snow, graupel, cloud water and cloud ice). For the microwave and sub millimetre part of the spectrum, these tables are generated using a stand alone module within RTTOV-SCATT and provide the optical properties (albedo, asymmetry and extinction) for each of the required channels from various sensors calculated over a range of Liquid Water Content (LWC) and temperature values (Geer *et al.*, 2021).

The current default setup for the hydrotables in RTTOV allows pre-defined ranges of LWC and temperature. This work investigates whether these ranges remain suitable and determines if the default settings should be changed to accommodate future work, such as the upcoming Ice Cloud Imager (ICI) (to be launched on-board the Metop - Second Generation (Metop-SG)) (Eriksson *et al.*, 2020). The experiments presented in the following sections are undertaken for JJA 2020 and DJF 2020/1 and changes to the hydrotables are applied to the following sensors (platforms): SSMIS (DMSP-F17), AMSR2 (GCOM-W), MWRI (FY-3D), GMI (GPM), AMSU-A (NOAA, EOS, METOP), MWHS2 (FY-3D), MHS (NOAA, METOP). These are passive experiments where no DA is undertaken.

4.2 Extending the Liquid Water Content Range

At RTTOV v13.0, the LWC range used in the hydrotables covers 10^{-6} to 10^{-2} kg m^{-3} (logarithmically spaced) (Geer *et al.*, 2021). However, there has been some concern that this has resulted in points with LWC $> 10^{-2}$ kg m^{-3} using the optical properties from the uppermost bin and therefore being assigned incorrectly. To test this, an experiment has been run with the number of bins extended so that the LWC range is now 10^{-6} to 10^{-1} kg m^{-3}.

The changes in the simulated TBs due to the extension of the LWC range are shown in Figure 24. The changes are extremely small (approx. 10^{-5} K) and their geographical extent is very limited, with less than 0.2 % of points changing for each SSMIS channel. The same holds true for all other sensors considered (listed in Section 4.1 above).

4.3 Extending the Temperature Range

At RTTOV v13.0, the hydrotable temperature range covers 204 K to 273 K (for frozen hydrometeors) and 234 K to 303 K (for liquid hydrometeors) (Geer *et al.*, 2021). However, analysis of the temperatures seen for a randomly picked cycle (2022-06-30T18) (see Figure 25) shows that, particularly for locations where the ice content of the cloud is non-zero (Figure 25 panel (c)), the temperature range is often exceeded (marked by the red vertical lines). While less than 1% of the data for each level exceeds the maximum temperature allowed by the hydrotables (273 K for frozen hydrometeors), this portion is much higher (up to 6%) for points below the minimum temperature (for model levels 60 to 67).

In addition to the data which is not within the current bounds of the hydrotable ranges, it is recognised

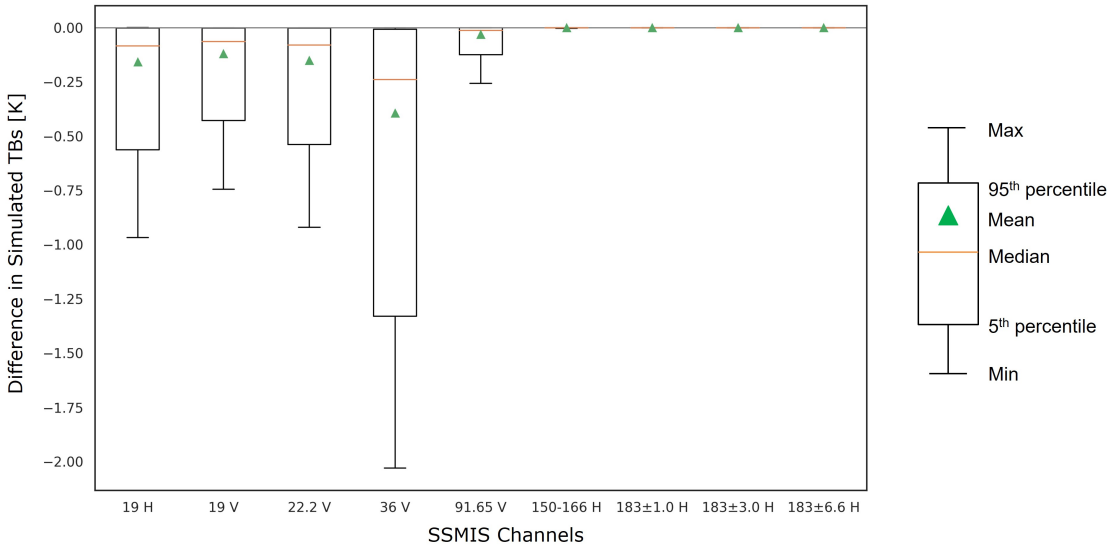

Figure 24: Change in the simulated TBs when the LWC range of the hydrotables is extended. Global statistics, for the period 2020-07-01 to 2020-07-31.

that the introduction of temperatures representing the melting layer (above 273 K) and associated bright band effect are important for RAdio Detection And Ranging (RADAR) simulations and the frequencies covered by ICI which will have increased sensitivity to the top (coldest) part of the cloud. Therefore, an experiment has been run which extends the temperature ranges of the hydrotables both upwards and downwards to the following: 178 K to 277 K (for frozen hydrometeors, previously 204 K to 273 K) and 214 K to 313 K (for liquid hydrometeors, previously 234 K to 303 K).

Note that, changing the temperature limits in this way results in some of the assumptions for the PSD (from Field *et al.* (2007)), being exceeded as well as potentially being outside of the limits for the optical assumptions from the ARTS database (although note Geer *et al.* (2021) shows that the hydrotables based on the ARTS database are valid down to 180 K). However, the majority of the changes in the simulated TBs (shown per channel of SSMIS-F17 in Figure 26) are of the order of magnitude 10^{-3}, with a very few points exceeding this level (although the 91.655v GHz channel shows some changes beyond -0.06 K). Geographically, the changes are very small but widespread in the SH temperate zone, with some larger magnitude changes in the tropics. Based on these results, it is considered that exceeding the assumptions detailed above has very little impact on the simulated TBs.

4.4 Inclusion within the ECMWF Operational IFS

As discussed above, the changes to the range of the hydrotables results in a very minimal difference to the simulated TBs when tested in the ECMWF-IFS, both for the LWC and temperature range extensions. In light of this, the increased storage requirements for the larger hydrotables and the minimal number of observations outside of the already utilised range, the new hydrotable ranges will not be implemented operationally in the ECMWF-IFS. Instead, the code which facilitates the hydrotable range extension will be included within the RTTOV v13.2 package, and an optional setting allows the use of range-extended hydrotables (both LWC and temperature ranges extended). This also allows for future developments in this direction and further facilitates RADAR simulations in RTTOV.

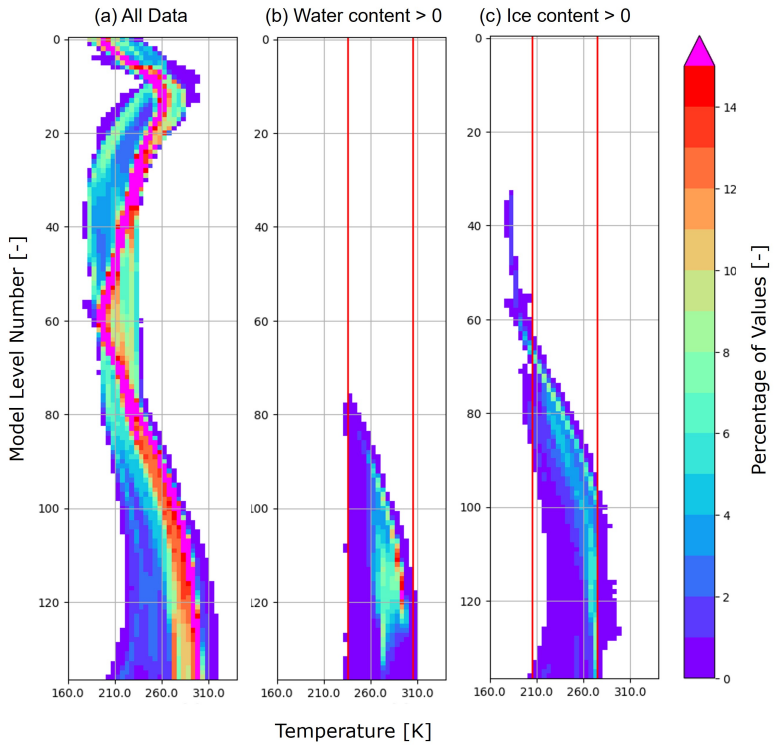

Figure 25: Percentage of values (for one level) falling in a 5 K bin shown for all model levels (where level 1 is the top of the atmosphere and 137 is the surface). All available data is shown in (a), those points where the corresponding water content is above 0 (a proxy for liquid hydrometeors) is shown in (b) and those points where the corresponding ice content is above 0 (a proxy for frozen hydrometeors) is shown in (c). The red vertical lines in (b) and (c) show the ranges of the hydrotables applied at RTTOV 13.0. Global statistics, for the 2022-06-30T00 cycle.

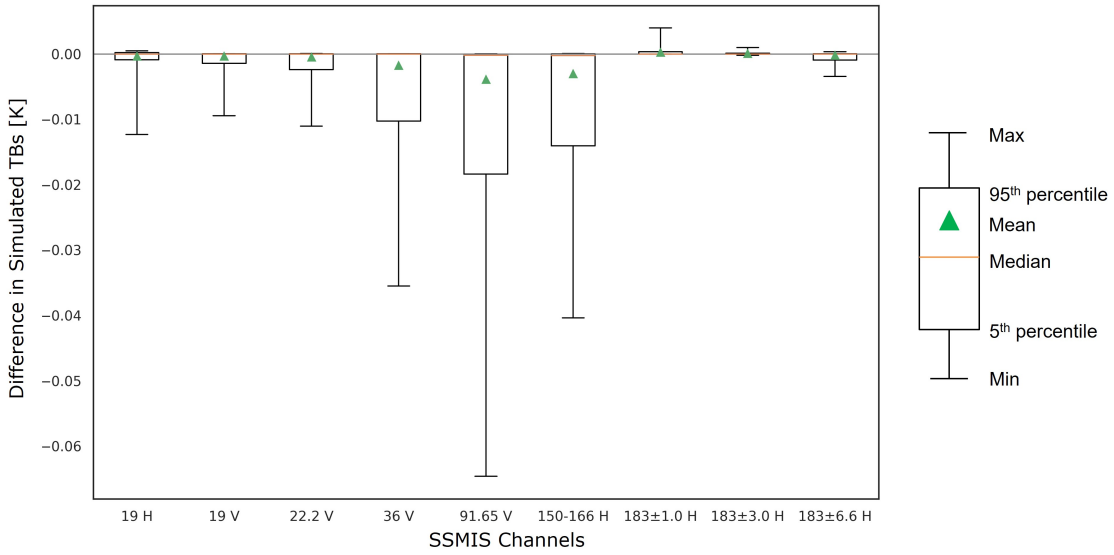

Figure 26: Change in the simulated TBs when the temperature range of the hydrotables is extended. Global statistics, for the period 2020-07-01 to 2020-07-31.

Acknowledgements

Tracy is supported by the EUMETSAT Fellowship Programme.

Regarding the extension of the RTTOV hydrotables, acknowledgement goes to Philippe Chambon, Rohit Mangla and Mary Borderies of Meteo-France for the extensive discussions related to this work.

Regarding the MWRI orbital biases, Wei Han and Shengli Wu of China Meteorological Administration are thanked for their discussions on this issue and for alerting ECMWF in the first instance.

References

Bauer, P., Geer, A. J., Lopez, P. and Salmond, D. (2010). Direct 4D-Var assimilation of all-sky radiances. Part I: Implementation. *Quarterly Journal of the Royal Meteorological Society*, **136**(652), 1868–1885, doi:https://doi.org/10.1002/qj.659, URL https://rmets.onlinelibrary.wiley.com/doi/abs/10.1002/qj.659.

Bell, W., English, S. J., Candy, B., Atkinson, N., Hilton, F., Baker, N., Swadley, S. D., Campbell, W. F., Bormann, N., Kelly, G. and Kazumori, M. (2008). The assimilation of SSMIS radiances in numerical weather prediction models. *IEEE Transactions on Geoscience and Remote Sensing*, **46**(4), 884–900, doi:10.1109/TGRS.2008.917335, URL https://ieeexplore.ieee.org/document/4468717.

Booton, A., Bell, W. and Atkinson, N. (2014). An improved bias correction for SSMIS.

Bormann, N., Lawrence, H. and Farnan, J. (2019). Global observing system experiments in the ecmwf assimilation system. *Technical Report 839*, doi:10.21957/sr184iyz, URL https://www.ecmwf.int/node/18859.

Cardinali, C. (2009). Monitoring the observation impact on the short-range forecast. *Quarterly Journal of the Royal Meteorological Society*, **135**(638), 239–250, doi:https://doi.org/10.1002/qj.366, URL https://rmets.onlinelibrary.wiley.com/doi/abs/10.1002/qj.366.

Dee, D. (2004). Variational bias correction of radiance data in the ECMWF system. In *ECMWF Workshop on Assimilation of high spectral resolution sounders in NWP, 28 June - 1 July 2004*, pp. 97–112, ECMWF, URL https://www.ecmwf.int/node/8930.

ECMWF (2017). Scientific Advisory Committee: 46th session: Agenda item 10.1: Assimilation of observations sensitive to cloud and precipitation. *Technical Report ECMWF/SAC/46(17)12*, ECMWF, URL https://www.ecmwf.int/en/about/who-we-are/governance/sac/46-0.

ECMWF (2021). *IFS Documentation CY47R3 - Part VI: Technical and computational procedures*. Number 6 in IFS Documentation, ECMWF, doi:10.21957/3oxwrgb0s, URL https://www.ecmwf.int/node/20200.

ECMWF (2022). Scientific Advisory Committee: 51st Session: Methods for assessing impact of current and future - components of the global observing system. *Technical Report ECMWF/SAC/51(22)5*, ECMWF.

Eriksson, P., Rydberg, B., Mattioli, V., Thoss, A., Accadia, C., Klein, U. and Buehler, S. A. (2020). Towards an operational Ice Cloud Imager (ICI) retrieval product. *Atmospheric Measurement Techniques*, **13**(1), 53–71, doi:10.5194/amt-13-53-2020, URL https://amt.copernicus.org/articles/13/53/2020/.

Field, P. R., Heymsfield, A. J. and Bansemer, A. (2007). Snow size distribution parameterization for midlatitude and tropical ice clouds. *Journal of the Atmospheric Sciences*, **64**(12), 4346 – 4365, doi:10.1175/2007JAS2344.1, URL https://journals.ametsoc.org/view/journals/atsc/64/12/2007jas2344.1.xml.

Geer, A. J. (2013). All-sky assimilation: better snow-scattering radiative transfer and addition of SSMIS humidity sounding channels. *Technical Report 706*, doi:10.21957/uxq5zlprk, URL https://www.ecmwf.int/node/9502.

Geer, A. J. (2021). Physical characteristics of frozen hydrometeors inferred with parameter estimation. *Atmospheric Measurement Techniques*, **14**(8), 5369–5395, doi:10.5194/amt-14-5369-2021, URL https://amt.copernicus.org/articles/14/5369/2021/.

Geer, A. J., Ahlgrimm, M., Bechtold, P., Bonavita, M., Bormann, N., English, S., Fielding, M., Forbes, R., Hogan, R., Hólm, E., Janiskova, M., Lonitz, K., Lopez, P., Matricardi, M., Sandu, I. and Weston, P. (2017). Assimilating observations sensitive to cloud and precipitation. *Technical Report 815*, doi:10.21957/sz7cr1dym, URL https://www.ecmwf.int/node/17718.

Geer, A. J. and Bauer, P. (2010). Enhanced use of all-sky microwave observations sensitive to water vapour, cloud and precipitation. *Technical Report 620*, doi:10.21957/mi79jebka, URL https://www.ecmwf.int/node/9518, also published as EUMETSAT/ECMWF RR20.

Geer, A. J. and Bauer, P. (2011). Observation errors in all-sky data assimilation. *Quarterly Journal of the Royal Meteorological Society*, **137**(661), 2024–2037, doi:https://doi.org/10.1002/qj.830, URL https://rmets.onlinelibrary.wiley.com/doi/abs/10.1002/qj.830.

Geer, A. J., Bauer, P. and Bormann, N. (2010a). Solar biases in microwave imager observations assimilated at ECMWF. *IEEE Transactions on Geoscience and Remote Sensing*, **48**(6), 2660–2669, doi:10.1109/TGRS.2010.2040186.

Geer, A. J., Bauer, P., Lonitz, K., Barlakas, V., Eriksson, P., Mendrok, J., Doherty, A., Hocking, J. and Chambon, P. (2021). Bulk hydrometeor optical properties for microwave and sub-millimetre radiative transfer in RTTOV-SCATT v13.0. *Geoscientific Model Development*, **14**(12), 7497–7526, doi:10.5194/gmd-14-7497-2021, URL https://gmd.copernicus.org/articles/14/7497/2021/.

Geer, A. J., Bauer, P. and Lopez, P. (2010b). Direct 4D-Var assimilation of all-sky radiances. Part II: Assessment. *Quarterly Journal of the Royal Meteorological Society*, **136**(652), 1886–1905, doi:https://doi.org/10.1002/qj.681, URL https://rmets.onlinelibrary.wiley.com/doi/abs/10.1002/qj.681.

Geer, A. J., Bauer, P. and O'Dell, C. W. (2009a). A revised cloud overlap scheme for fast microwave radiative transfer in rain and cloud. *Journal of Applied Meteorology and Climatology*, **48**(11), 2257 – 2270, doi:10.1175/2009JAMC2170.1, URL https://journals.ametsoc.org/view/journals/apme/48/11/2009jamc2170.1.xml.

Geer, A. J., Forbes, R. and Bauer, P. (2009b). Cloud and precipitation overlap in simplified scattering radiative transfer. *Technical Report 18*, ECMWF, URL https://www.ecmwf.int/node/9516.

Geer, A. J., Lonitz, K., Duncan, D. and Bormann, N. (2022). Improved surface treatment for all-sky microwave observations. *Technical Report 894*, doi:10.21957/zi7q6hau, URL https://www.ecmwf.int/node/20337.

Kroodsma, R., Berg, W. and Wilheit, T. (2021). Updates to the special sensor microwave imager/sounder (ssmis) calibration for the gpm v07 data release. In *2021 IEEE International Geoscience and Remote Sensing Symposium IGARSS*, pp. 7748–7751, doi:10.1109/IGARSS47720.2021.9553213, URL https://ieeexplore.ieee.org/document/9553213.

Kunkee, D. B., Swadley, S. D., Poe, G. A., Hong, Y. and Werner, M. F. (2008). Special sensor microwave imager sounder (ssmis) radiometric calibration anomalies—part i: Identification and characterization. *IEEE Transactions on Geoscience and Remote Sensing*, **46**(4), 1017–1033, doi:10.1109/TGRS.2008.917213, URL https://ieeexplore.ieee.org/abstract/document/4475707.

Lean, P., Geer, A. J. and Lonitz, K. (2017). Assimilation of Global Precipitation Mission (GPM) microwave imager (GMI) in all-sky conditions. *Technical Report 799*, doi:10.21957/8orc7sn33, URL https://www.ecmwf.int/node/17174.

Lean, P., Hólm, E. V., Bonavita, M., Bormann, N., McNally, A. P. and Järvinen, H. (2021). Continuous data assimilation for global numerical weather prediction. *Quarterly Journal of the Royal Meteorological Society*, **147**(734), 273–288, doi:https://doi.org/10.1002/qj.3917, URL https://rmets.onlinelibrary.wiley.com/doi/abs/10.1002/qj.3917.

Saunders, R., Hocking, J., Turner, E., Havemann, S., Geer, A., Lupu, C., Vidot, J., Chambon, P., Kopken-Watts, C., Scheck, L., Stiller, O., Stumpf, C. and Borbas, E. (2020). RTTOV-13: Science and validation report. URL https://nwp-saf.eumetsat.int/site/download/documentation/rtm/docs_rttov13/rttov13_svr.pdf.

Saunders, R., Hocking, J., Turner, E., Rayer, P., Rundle, D., Brunel, P., Vidot, J., Roquet, P., Matricardi, M., Geer, A., Bormann, N. and Lupu, C. (2018). An update on the RTTOV fast radiative transfer model (currently at version 12). *Geoscientific Model Development*, **11**(7), 2717–2737, doi:10.5194/gmd-11-2717-2018, URL https://gmd.copernicus.org/articles/11/2717/2018/.

Swadley, S. D., Poe, G. A., Baker, N., Ruston, B., Bell, W., Kunkee, D. B. and Boucher, D. (2010). SSMIS radiance assimilation, calibration anomaly mitigation and assimilation results from F18.

WMO (2022a). Details for instrument MWRI. URL https://space.oscar.wmo.int/instruments/view/mwri.

WMO (2022b). Details for instrument SSMIS. URL https://space.oscar.wmo.int/instruments/view/ssmis.

WMO (2022c). Space-based capabilities. URL https://space.oscar.wmo.int/spacecapabilities.